Direct simulation of turbulent swept flow over a wire in a channel

By R. RANJAN[1]†, C. PANTANO[1] and P. FISCHER[2]

[1]Department of Mechanical Science and Engineering,
University of Illinois at Urbana-Champaign,
1206 W. Green St., Urbana, IL, 61801, USA.
[2]Mathematics and Computer Science Division,
Argonne National Laboratory,
Argonne, IL, 60439, USA.

(Received 27 March 2009)

The turbulent swept flow around a cylindrical wire resting on a wall of a channel is investigated using direct numerical simulation. This geometry is a model of the flow through the wire-wrapped fuel pins, the heat exchanger, typical of many reactor designs. Mean flow along and across the wire axis is imposed, leading to the formation of separated and reattached secondary flow regions. The Reynolds number based on the centerline velocity along the wire axis direction is 6000 and four cases are simulated with different flow rates across the wire. This configuration is topologically similar to backward-facing steps or slots with swept flow, except that the dominant flow is along the obstacle axis in the present study and the cross flow is smaller than the axial flow, i.e. large swept. Mean velocities, turbulence statistics, wall shear stress probability distribution functions and instantaneous flow structures are investigated. Particular attention is devoted to the statistics of the shear stress on the walls of the channel and wire in the recirculation zone. The effect of cross-flow strength on the statistics is discussed. The flow around the mean reattachment region, at the termination of the recirculating bubble, does not exhibit the typical decay of the mean shear stress observed in classical backward facing step flow as one approaches this region owing to the presence of a strong axial flow. There is, nevertheless, a change in the mean angle of the wall shear stress from the external to the recirculation region. Normalized probability density functions of wall shear stress exhibit a weak dependence across the wall of the channel. This is consistent with the presence of strong axial flow, which keeps the flow highly turbulent irrespective of the strength of the cross-flow, except within the secondary flow regions that appear to laminarize.

1. Introduction

Heat transfer over turbulent flows with separation, in particular recirculating flows, has a long history (Kays & Crawford 2004). Understanding the statistics of these flows, which include reattachment length and internal structure of the recirculation bubble, and the structure of the small turbulent scales is of fundamental interest. These types of flows are generated by various factors, including geometrical complexity, presence of adverse pressure gradient and skewness of the flow. They exhibit flow separation, presence of shear layers, reattachment and flow recovery. Each of these phenomena has a distinct character and shows a high degree of variability between cases. Still one can

† Corresponding author: rranjan2@illinois.edu

classify such turbulent flows into two categories, namely, those with separation or with turbulence induced secondary flows. Different features of two- and three-dimensional turbulent boundary layer separation is reviewed in detail by Simpson (1996).

In this paper, we investigate the turbulent flow in a channel where a circular wire has been placed over one of the walls using direct numerical simulation (DNS). In particular, there is mean flow along both the axial direction of the wire and across it. This cross-flow scenario has not been exhaustively investigated in the past, although it represents a first order geometrical simplification of turbulent flows along complex wire-wrapped assemblies, e.g. utilized in some nuclear reactors. The purpose of using wire-wrapped assemblies is to enhance mass transfer, heat transfer and mixing in several industrial and chemical processes. In the presence of cross-flow, the recirculation flow behind the wire is not closed in the mean since axial flow is also present. A review of DNS as a research tool to simulate turbulent flows is provided by Moin & Mahesh (1998) and a discussion of applicability of DNS to such complex flows is provided by Karniadakis (1999). Some examples of recent simulation of turbulent flow in complex geometry and engineering flows include the DNS of turbulent flow in a stationary and serpentine passage by Laskowski & Durbin (2007), of a round turbulent jet in a laminar cross flow by Muppidi & Mahesh (2007), and flow through low-pressure turbine cascades by Rodi (2006).

The canonical flows exhibiting recirculation features include flow over a backward-facing step, forward-facing step, surface mounted rib, bump on a surface, half cylinder and channel with a constriction. The most studied flow is the backward facing step where a separation bubble exists owing to an abrupt change in geometry or pressure gradient. Backward-facing step flow has been studied in great detail in the past owing to its geometrical simplicity. A detailed review has been offered by Bradshaw & Wong (1972) and later by Eaton & Johnston (1981). As mentioned by Bradshaw & Wong (1972) and Simpson (1996), a key feature of this flow is its slow monotonic return of the shear layer to the ordinary boundary layer flow after reattachment and an important characteristic of this flow is the prediction of the reattachment length of the primary separation bubble (Eaton & Johnston 1981). Armaly *et al.* (1983) studied the effect of Reynolds number on reattachment length, both experimentally and numerically, and found that it increases in the laminar regime, decreases in the transitional regime and remains nearly constant in the turbulent regime. Adams & Johnston (1988) showed a reduction in reattachment length when the boundary layer upstream of separation is laminar compared to turbulent and attributed it to a high shear layer entrainment. Shih & Ho (1994) performed experimental measurements in a low aspect ratio configuration and found that reattachment length and the flow in the recirculating region is highly three-dimensional and also proposed that the reattachment length indicates the level of entrainment from the shear layer. A detailed numerical investigation by Le *et al.* (1997) showed the unsteady characteristics of this flow in terms of variation of reattachment length, presence of high turbulent activity regions near reattachment and slow recovery after reattachment. Dejoan & Leschziner (2004) performed large-eddy simulation (LES) of a periodically perturbed separated flow over a backward-facing step and found that perturbations lead to a reduction in reattachment length and it also enhanced the rate of recovery owing to enhanced turbulent activity in the recirculating region. The stability analysis for this flow configuration has been carried out numerically by Dwight *et al.* (2002), Sheu & Rani (2006) and Rani *et al.* (2007). Dwight *et al.* (2002) showed that three-dimensional instability is associated with the primary recirculating region which is controlled by a centrifugal mechanism. Sheu & Rani (2006) showed that periodic behavior of reattachment length is closely associated with hovering vortical structures present below the separated shear layer and three dimensionality of the flow is observed

in terms of presence of complex vortical structures. Rani *et al.* (2007) studied the role of Kelvin-Helmholtz instability and Taylor-Görtler-like vortices on unsteadiness and three-dimensionality of this flow. Kaiktsis & Monkewitz (2003) studied global destabilization of two-dimensional flow over a backward facing step by inducing suction at the step face to enhance local absolute instability and blowing at opposite wall to reduce non-parallelism and found that flow acquires unsteadiness in the form of a time periodic state having an array of traveling vortices which depends on the streamwise extent of blowing and its location from the step. Flow over a forward facing step has been studied experimentally by Farabee & Casarella (1986) and Camussi *et al.* (2008) and numerically by Wilhelm *et al.* (2003). The significant characteristic of this flow is presence of two recirculating regions, one upstream of the step and another downstream of the step. This flow also shows slow recovery of the boundary layer after reattachment. Farabee & Casarella (1986) observed that the dynamics in the near reattachment region is different from that observed in the backward facing step, as there is no impingement on the wall in this case. Camussi *et al.* (2008) showed that downstream reattachment length depends on Reynolds number whereas upstream reattachment length is less sensitive. Wilhelm *et al.* (2003) performed linear stability analysis at laminar Reynolds number and found that the transition from two to three dimensional state is a reaction of the flow to oncoming three dimensional disturbances and is not related to an absolute instability. Achraya *et al.* (1994) and Hwang *et al.* (1999) performed a computational study of turbulent flow past a surface mounted two-dimensional rib. Achraya *et al.* (1994) reported non equilibrium of turbulence kinetic energy in the recirculation region and shear layer which extends after reattachment and mentioned that production and dissipation terms become significant in the separated regime. Hwang *et al.* (1999) studied the effect of varying rib length on the flow and found that the recirculation length upstream and downstream of the rib was insensitive and sensitive to the length of the rib, respectively. Liua *et al.* (2008) performed experimental investigation of turbulent flow over a two-dimensional rib and found high turbulence intensity in the shear layer, which decays slowly after reattachment of flow. The velocity profile downstream of reattachment point indicated incomplete flow recovery.

Other studies have concentrated on the effect of curved walls on turbulence. Wu & Squires K. (1998) have performed LES of a boundary layer over a smooth bump and confirmed the presence of an internal layer over the bump surface. They showed that perturbations in pressure gradient and surface curvature enhances near wall shear production of turbulence stresses and causes the formation of internal layers. Mittal *et al.* (2003) performed a numerical study of pulsatile flow in a channel with one-sided semi-circular constriction using DNS and LES and found shear layers, vortex shedding and recirculating regions. They studied the effect of Reynolds number and provided an empirical relation between Reynolds number and shedding frequency. Marquillie & Ehrenstein (2003) examined the mechanism of onset of instability in separated boundary layer flow created by a smooth bump on a flat plate and found that the flow becomes structurally stable near reattachment region above a critical Reynolds number and low frequency oscillations associated with a global instability. Gallaire *et al.* (2007) used DNS of flow over a bump with no side walls to analyze the three-dimensional instabilities and observed a stationary transverse instability in the primary recirculating region. They used stability analysis to interpret the formation of longitudinal structures in the flow. Griffith *et al.* (2007) also performed stability analysis of the flow in a partially blocked channel having a constriction on one of the channel walls and found that a stationary instability mode lies in the primary recirculating region, which was attributed to an elliptic instability. Marquillie *et al.* (2008) performed a DNS study of flow over a smooth curved surface on a

channel and found that the separated regime is characterized by disappearance of streaky structures, which reappear further downstream after reattachment. The begining of the separation bubble is characterized by low levels of turbulence kinetic energy compared to the downstream part of the bubble where small vortices interact with large structures convecting into the boundary layer.

In other studies, recirculation regions are produced over turbulent boundary layer by means of adverse pressure gradients. These flows are devoid of curvature effects and isolate phenomena associated with the separation of the flow. Wood & Bradshaw (1982) studied experimentally the effect of a wall on a turbulent mixing layer and observed a significant change in the turbulence structure of the mixing layer before changes occurred in the velocity profile. Kiya & Sasaki (1985) studied experimentally unsteadiness of reverse flow over a blunt plate having a separated bubble and found that low frequency unsteadiness is associated with large scales of flow. Dianat & Castro (1991) performed detailed measurements of turbulent quantities within a separated flow over a flat plate turbulent boundary layer subjected to adverse pressure gradient and highlighted that Reynolds stresses are very anisotropic near the reattachment region. Honkan & Andreopoulos (1997) measured vorticity, strain-rate, dissipation and invariants of the strain-rate tensor and velocity gradient tensor and observed strong Reynolds number dependence in near wall quantities. Spalart & Coleman (1997) performed a DNS study of a separation bubble created by suction and blowing and analyzed in detail several physical quantities like, wall shear stress, skin friction, heat transfer, turbulence intensities and turbulence kinetic energy and found that weakening of wall blocking effect occurs owing to lifting of fluid away from the wall. Na & Moin (1998) performed a detailed and extensive DNS study of a separated turbulent boundary layer and reported highly three-dimensional behavior of separation and reattachment regions. Spalart & Strelets (2000) performed a DNS study of transitional flow having a separated bubble and observed highly three dimensional flow near separation while the logarithmic law was not observed in separated and relaxation regions of the flow. Caruelle (2003) performed detached eddy simulation of detached boundary layers and observed a modified logarithmic law for the mean velocity profile in the separated region. Angele & Muhammad-Klingmann (2006) studied weakly separating and reattaching turbulent boundary layers experimentally and found that the logarithmic region vanishes in the separated region owing to adverse pressure gradient. Deck & Thoringy (2007) used the zonal detached eddy simulation method to study axisymmetric separating/reattaching flow and observed that the recirculation bubble interacts with external flow through the shear layer mixing. Finally, Sadeque *et al.* (2008) performed an experimental study of flow around cylinders in open channel with different level of submergence and analyzed deflected mean flow in terms of three-dimensional turbulent boundary layer cross flow models. A number of studies concentrating on the measurements of wall pressure have been carried out for backward and forward facing steps, turbulent boundary layers and bumps (Farabee & Casarella 1986; Snarski & Lueptow 1995; Nepomuceno & Lueptow 1997; Lee & Sung 2002; Hudy *et al.* 2003; Chun *et al.* 2004; Liu *et al.* 2005; Hoarau *et al.* 2006; Kim & Sung 2006; Hudy *et al.* 2007; Camussi *et al.* 2008). In all these studies it was reported that separation and reattachment of flow produces large amplitude and low frequency pressure fluctuations. This causes a sharp rise in root mean square (r.m.s.) of wall pressure near the reattachment point. It was also observed that peak of positive fluctuations are associated with acceleration of streamwise flow and negative peaks are associated with deceleration of flow. The common theme that has emerged in study of these flows is that curvature, adverse or favorable pressure gradients and impingement of the shear layers on the walls affect in important

manners the overall flow dynamics and mean turbulence quantities. All these effects are present in the flow considered in this study in addition to the effect of the swept angle.

Fewer studies have concentrated on swept flow. The secondary flow does not lead to a closed separation bubble owing to simultaneous presence of mean flow in both the streamwise and spanwise directions. Johnston (1970) studied three-dimensional turbulent boundary layer induced by swept forward-facing steps experimentally and demonstrated that substantial deviation occurs between the turbulent shear stress vector and velocity gradient vector. Bradshaw (1987) reviewed experimental works related to turbulent secondary flows which can be stress induced or by skewing of pre-existing shear layers and discussed the need to improve modeling of pressure strain and turbulent transport. Weber & Danberg (1992) performed experimental measurements of mean velocity in flow over a swept backward-facing step which is a simple representation of three-dimensional flow and found that boundary layer thickness increases with increase in sweep angle. Moreover, in the reattachment region, the Cole's wake parameter becomes significant owing to the disappearance of the inner or wall layer. Lu & Lele (1993) studied effect of skewing on inviscid instability of a compressible mixing layer and showed that skewing can have destabilizing effects on the flow owing to increase in velocity ratio and stabilizing effects owing to increase in convective Mach number. Webster *et al.* (1996) studied the combined effect of surface curvature, streamwise pressure gradient and mean cross flow on a swept bump and found that the turbulent shear stress vector lags the velocity gradient vector and vertical mixing is not suppressed owing to addition of mean cross flow. Kaltenbach & Janke (2000) performed DNS of flow separation behind a swept rearward-facing step by varying sweep angle between 0^o to 60^o and found that reattachment length reduces up to 50% for high sweep angles. In this study, the flow is highly three dimensional owing to existence of transverse pressure gradient and transverse shear and sweep independence of flow exists for sweep angles up to 40^o. Kaltenbach (2003) used DNS of the flow behind a swept backward-facing step to study effect of skewing on turbulence structure and identified origin of axial vorticity and provided details of strain field. They found that strain induced stretching-compression and skewing of mean flow influences turbulence structure only in the vicinity of separation. In most of these studies, the amount of sweep varies from 0^o to 60^o.

Unfortunately, less is known of the remaining cases, i.e. large swept, which could be considered on their own right more appropriately as turbulent cross flows. This is the main objective of the present study, where the cross flow is varied between 0^o and approximately 19^o, based on the average velocity, or between 71^o and 90^o in terms of swept angles. One noticeable difference between these flows and other backward facing step flows is that the flow within the recirculation region is always fully turbulent, owing to the presence of a large axial flow. The objective of the present study is to understand the nature of the mean flow, obtain turbulence statistics, analyze the shear stress distribution and instantaneous flow structures around the region of recirculation. This paper is organized as follows. Section 2 describes the problem and associated parameters. Details of computational method is provided in §3. Turbulence statistics are discussed in §5. Analysis of shear stress distribution is done in §7 and §4 discusses instantaneous flow structures. The paper ends with a short summary in §8.

2. Flow description

The problem considered in this study corresponds to a channel with a wire sitting along one of its walls. A schematic of the problem is shown in the figure 1. The domain extends $L_x \times 2h \times L_z = 4\pi \times 2 \times 8\pi$ in the x, y and z directions, respectively. The x coordinate

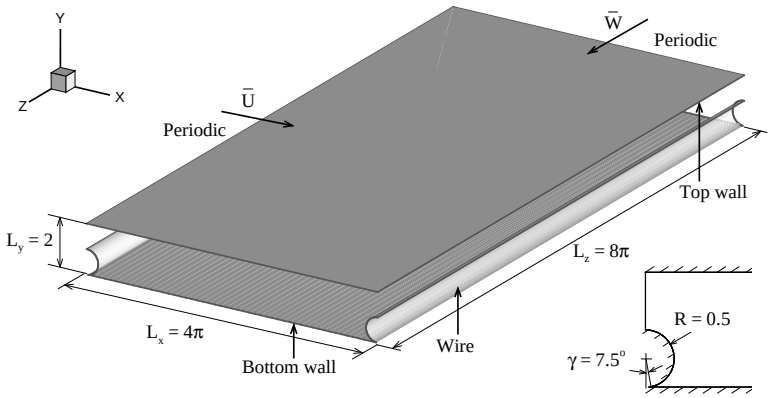

FIGURE 1. Schematic of the geometry considered in the present study.

denotes the cross flow direction, y is the vertical direction and z is the streamwise or axial direction. Periodic boundary conditions are employed along the cross flow and streamwise directions and the no-slip boundary condition is used at the walls and at the surface of the wire. For convenience, the center of the cylindrical wire of radius $R = 0.5$ is placed at the boundary of the periodic domain and it is aligned with the x axis. Previous studies of flow in a periodic channels with hills by Mellen *et al.* (2000), Fröhlich *et al.* (2005) and Peller & Manhart (2006) suggest that good streamwise decorrelation and complete flow reattachment is observed using streamwise periodic boundary conditions if $L_x/h \geq \pi$, where h denotes the hill (obstacle) height. Therefore, in the present study, the cross-flow length of the domain was chosen as $L_x = 4\pi$.

In practical wire-wrapped assemblies, the wire is wrapped under tension around a nuclear fuel pin and there is a slight deformation of the wire at the contact location. To approximately model this detail we have chosen to impose a finite contact angle between the wire and the wall. Therefore, the contact half-angle of the wire with the bottom wall of the channel is $\gamma = 7.5^o$, see right-bottom inset in figure 1. The flow in the channel is driven by the pressure gradient resulting from imposed constant flowrates along the axial and cross flow directions. In this study, the flowrate specified in the axial direction is generally higher than that imposed in the cross flow direction. The resulting cross flow over the wire produces a large recirculation region or bubble with mean axial flow in the lee side of the wire. The flow detaches from the top surface of the wire, a shear layer is formed over a recirculation zone that finally reattaches some distance downwind from the wire.

3. Mathematical formulation, approach and parameters

3.1. *Governing equations and numerical method*

The motion of an incompressible fluid with constant density, ρ, and constant viscosity, μ, is governed by the Navier-Stokes equations,

$$\frac{\partial \boldsymbol{u}}{\partial t} = \boldsymbol{N}(\boldsymbol{u}) - \boldsymbol{\nabla} p + \frac{1}{Re}\nabla^2 \boldsymbol{u}, \tag{3.1}$$

and the continuity equation

$$\boldsymbol{\nabla}.\boldsymbol{u} = 0, \tag{3.2}$$

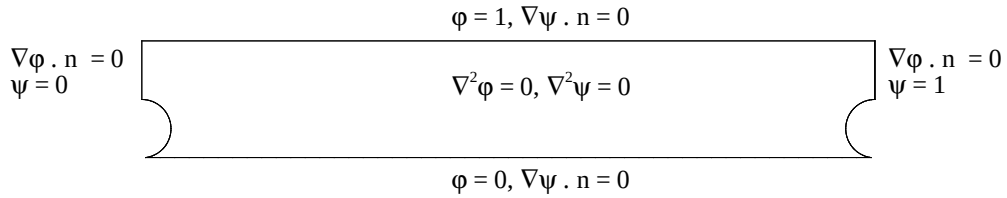

FIGURE 2. Two dimensional cross-section of the domain.

in the computational domain Ω, where $\boldsymbol{u} \equiv (u, v, w)$ represents the velocity field, p is the pressure, and

$$Re \equiv \frac{\rho U L}{\mu},$$

is the Reynolds number. The above equations are written in non-dimensional form using U as the characteristic velocity scale and L as the characteristics length scale. The term $\boldsymbol{N(u)}$ represents the non-linear advection term, given by

$$\boldsymbol{N(u)} = -\frac{1}{2}[(\boldsymbol{u}.\boldsymbol{\nabla})\boldsymbol{u} + \boldsymbol{\nabla}.(\boldsymbol{uu})]. \tag{3.3}$$

This particular skew-symmetric form of $\boldsymbol{N(u)}$ has been shown by Zang (1991) to be more robust compared to other forms that are equivalent in the continuous case, e.g. convective and rotational forms, when the governing equations are discretized. In particular, this form minimizes aliasing errors of the spectral spatial discretization used in this study to solve the governing equations.

Time dependent simulations based on the above set of equations are carried out using a spectral element method implemented in *Prism* (Henderson 1994). The equations are discretized using two-dimensional spectral elements in the x-y plane and Fourier modes in the axial direction. In the spectral element method, the domain Ω is subdivided into K macro elements. Within each of these K elements the geometry and the solution variables are represented by using N^{th} order tensor-product polynomial expansions as basis functions. These basis function are Gauss-Lobatto Legendre (GLL) polynomial interpolants. A third order accurate time-splitting scheme developed in Karniadakis *et al.* (1991) is used to integrate the above set of equations. The splitting scheme leads to a set of equations comprising of an advection equation, and a sequence of elliptic Helmholtz equations enforcing the incompressibility constraint and the linear viscous term present in the semi-implicit time integration. The advection terms are treated explicitly in this approach while the system of implicit elliptic Helmholtz equations are solved by a direct method using static condensation. Henderson & Karniadakis (1995) provides more details of the method and the solution strategy.

3.2. *Mesh properties*

The computational mesh comprises of macro spectral elements where each element is resolved by a high-order polynomial basis function. The mesh conforms to the boundary shape to enhance accuracy and improve convergence. The macro elements are determined as follows. First, two scalars functions, denoted φ and ψ, obeying Laplace equation in the domain shown in figure 2 are solved with two different sets of boundary conditions. Dirichlet boundary conditions are specified along the walls for scalar φ, with a value of $\varphi = 0$ on the bottom wall including the wire and $\varphi = 1$ on the top wall. Homogeneous Neumann conditions are specified at the periodic boundaries. Homogeneous Neumann conditions are specified at all walls and Dirichlet conditions are specified for scalar ψ,

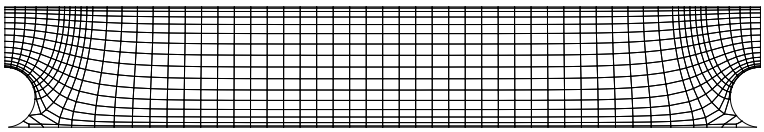

FIGURE 3. Macro spectral elements in the $x - y$ plane.

Case	Re_z	Re_x	Re_b	Re_τ	Q_z	Q_x
A	6000	0	6000	305	21.93	0
B	6000	500	6021	307	21.93	3.49
C	6000	1000	6083	312	21.93	7.05
D	6000	2000	6325	335	21.93	14.32

TABLE 1. Simulation parameters for all cases.

with a value of $\psi = 0$ and $\psi = 1$, along periodic boundaries, respectively. The new functions are used to construct a curvilinear mapping defined by the iso-lines of φ and ψ.

Appropriately spaced iso-levels of φ and ψ are then used to construct logically quadrilateral macro spectral elements, defined by the co-ordinates of the intersection of these iso-levels. The elements at the corners regions, where the wire contacts the wall, were modified manually to improve their quality. The resulting final mesh is shown in figure 3. After a few iterations and simulations, a mesh containing a total of 936 macro elements in the $x - y$ plane was selected. Each of these elements are further resolved by a 15^{th} order GLL polynomial. A total of 512 Fourier modes are used in the homogeneous z direction, resulting in an overall 107,827,200 collocation points. This mesh was found to be sufficiently accurate to resolve all the flows considered in this study. This was verified by determining the inner-scaled mesh spacing using the axial flow velocity, which is constant in all simulations. A non-uniform wall-normal spacing of the elements is used to ensure a higher density of mesh points close to the walls. The first mesh point away from the wall is located at $y^+ \approx 0.13$ and maximum spacing at the center line of the channel is 4.3 wall units. A non-uniform spacing is also used in the x direction with a minimum grid spacing of $\Delta x^+ \approx 2$ close to the wire and a maximum grid spacing of $\Delta x^+ \approx 6$ in the center of the domain.

3.3. *Simulation parameters*

Four different cases, labeled A through D, are investigated. The first case, A, has no cross flow over the wire and is considered as a reference scenario to compare with the other cases with cross flow, where a recirculation bubbles are present. The cross flowrate is increased from case B to D to investigate the effect of the wire and the amount of cross flow on the overall flow behavior. All statistical quantities in the flow studied here depend on the x and y coordinates. The z- and time-averaged mean of a flow quantity $\phi(x, y, z, t)$ is denoted by $\langle\phi\rangle$ and is defined as follows,

$$\langle\phi\rangle(x, y) = \frac{1}{N}\sum_{i=1}^{N}\left(\frac{1}{L_z}\int_0^{L_z}\phi(x, y, z, t_i)dz\right), \tag{3.4}$$

where L_z is the length of the domain in the homogeneous axial direction, i denotes a particular instant of time and N is the total number of time steps used to compute the average. These running averages are determined only after the simulations reach a

statistically steady state, as discussed below. The flowrates are defined in the customary manner, according to

$$Q_z = \iint_S W(x,y)dxdy, \tag{3.5}$$

where S denotes the $x-y$ cross section of the domain and

$$Q_x = L_z \int U(x,y)dy, \tag{3.6}$$

with $\langle u \rangle = U$ and $\langle w \rangle = W$ denoting the average cross flow and streamwise velocity component, respectively. Note that Eq. (3.6) is independent of x when the flow is statistically stationary, according to the continuity equation Eq. (3.2). In the present problem, mean flow occurs in both axial as well as cross flow directions. This is similar to three-dimensional turbulent boundary layers with crossflow inhomogeneity. The angle formed between the mean streamline and cross flow wall shear stresses is defined as the local net flow direction, given by

$$\theta = \tan^{-1}\left(\frac{\langle \tau_{mn} \rangle_{\mathrm{w}}}{\langle \tau_{ln} \rangle_{\mathrm{w}}}\right), \tag{3.7}$$

where $\langle \tau_{mn} \rangle$ and $\langle \tau_{ln} \rangle$ denote the shear stresses and subscript w denotes the value at the wall. The directions $\vec{m}$, $\vec{n}$ and $\vec{l}$ form a right-handed orthogonal system. On the walls of the channel, $\vec{m}$, $\vec{n}$ and $\vec{l}$ are aligned with the x, y and z axis, respectively. On the surface of the wire, $\vec{l}$ is aligned with the z axis, m is aligned with the azimuthal direction and n is aligned with the radial direction. A new orthogonal coordinate system $(s-q-n)$ can be obtained by rotating the $(l-m-n)$ system about the n axis. The new s coordinate is along the direction defined by θ, while q is oriented along the orthogonal direction to s. This direction for the local net flow direction is identical to the wall shear stress coordinate system introduced by Simpson (1996) for a three-dimensional turbulent boundary layer along which near-wall similarity exists for mean velocity. Moreover, under some circumstances, it is possible that a semi-log composite relationship may exist for the velocity profile along this direction. Simpson (1996) has shown that the wall shear stress vector is also aligned closely with the turbulent shear stress vector. As reported in other studies (Johnston 1970; Bradshaw 1987; Webster *et al.* 1996), the turbulent shear stress vector is not aligned with velocity gradient vector, which is an assumption built into isotropic eddy viscosity models. Thus, the net mean flow is represented by V_s along direction s in the new system and is given as follows,

$$V_s = \langle w \rangle \cos\theta + \langle u \rangle \sin\theta. \tag{3.8}$$

Additionally, the flow is characterized in both the axial and cross flow directions using the Reynolds number based on the channel half-height. These are given by

$$Re_z = \frac{\rho W_b h}{\mu}, \tag{3.9}$$

and

$$Re_x = \frac{\rho U_b h}{\mu}, \tag{3.10}$$

where $U_b = Q_x/(hL_z)$ and $W_b = Q_z/S$. The bulk Reynolds number is defined as

$$Re_b = \sqrt{Re_x^2 + Re_z^2}, \tag{3.11}$$

and the friction Reynolds number is given by

$$Re_\tau = \frac{\rho u_\tau h}{\mu}, \tag{3.12}$$

where

$$u_\tau = \sqrt{\frac{\overline{\tau}_\mathrm{w}}{\rho}}, \tag{3.13}$$

is the friction velocity and $\overline{\tau}_\mathrm{w}$ is the overall average shear stress at the walls. Owing to the presence of the wire and its induced secondary flows, a local average wall shear stress can be defined along direction s, similar to Simpson (1996) and Kaltenbach (2003), given by

$$\tau_\mathrm{w} = \langle \tau_{ln} \rangle_\mathrm{w} \cos\theta + \langle \tau_{mn} \rangle_\mathrm{w} \sin\theta. \tag{3.14}$$

This is also the maximum shear stress on the wall at any particular location. The overall average shear stress used in Eq. (3.13) is given by

$$\overline{\tau}_\mathrm{w} = \frac{1}{S_\mathrm{top} + S_\mathrm{bot}} \left(\iint_{S_\mathrm{top}} \tau_\mathrm{w} dS + \iint_{S_\mathrm{bot}} \tau_\mathrm{w} dS \right), \tag{3.15}$$

where S_bot and S_top denote the bottom wall including the wire surface and the top wall, respectively.

Four simulations are investigated in this study with identical flowrate in the axial direction and varying flowrates in the cross flow direction. Table 1 lists some of the parameters of these simulations, including all the Reynolds numbers defined above. Case A has no cross flow whereas the other cases have increasing amounts of cross flow. The initial flow field of case A is generated by imposing harmonic perturbations of 20% intensity over a parabolic velocity profile of the specified flowrate. The flow evolves until a fully developed and statistically stationary turbulent state is reached. This is verified by monitoring that the first- and second-order statistics as well as the wall-averaged shear stress, τ_w, ceases to change with time. The fully developed flow for case A is then used as the initial condition for case B. The initial flow field of case B evolves again through a transient period until it reaches a statistical stationary state. Statistics are gathered after this transient has passed. Proceeding in similar fashion, the initial flow fields for case C and D are obtained from the fully developed flow fields of case B and C, respectively.

4. Instantaneous flow structures

A recirculation bubble is characterized by the presence of rolled up vortices near the separation zone and three dimensional structures near the reattachment of the shear layer (Eaton & Johnston 1981; Chun & Sung 2003). Entrainment in the shear layer is associated with the reattachment length (Adams & Johnston 1988). It has also been observed in backward-facing step by Song & Eaton (2004) that turbulence is far from equilibrium near the reattachment zone owing to impingement of vortical structures, emanating from the shear layer, on the wall. Nepomuceno & Lueptow (1997) have associated wall pressure fluctuation to large scale vortical structures in the outer part of the boundary layer and small scale motions in the boundary layer. As mentioned in § 1, wall-pressure fluctuations are considered to be indicative of vortices being convecting over the wall (Liu *et al.* 2005) and has been used to study the structures present in the flow. Thus instantaneous flow structures reveals physical aspects of the flow, e.g. separation, reattachment and recovery, and it is used commonly for this purpose.

The λ_2-vortex criterion of Jeong & Hussain (1995) is adopted in order to investigate

some of the instantaneous small-scale structures observed in the flow. According to this criterion, a vortex core is defined as a region having net vorticity and simultaneously excluding regions of potential flow. It is also required that the geometry of the vortex core should be Galilean invariant. The λ_2 criterion identifies vortex cores by capturing local pressure minimum in a plane perpendicular to the vortex axis owing to vortical motion only. It eliminates the effect of viscous terms and unsteady irrotational motion, which may also cause a region of local pressure minimum. Thus, it is more insightful compared to other criteria, e.g. positive Q (second invariant of velocity gradient tensor), iso-contours of vorticity magnitude or local pressure minimum. The λ_2 criterion states that the second largest eigenvalue of the symmetric tensor $\boldsymbol{S}^2 + \boldsymbol{\Omega}^2$ must be negative in order for the local flow field to correspond to a vortex core. Here $\boldsymbol{S}$ and $\boldsymbol{\Omega}$ represents the strain rate and rotation tensor, respectively, and are defined by

$$S_{ij} = \frac{1}{2}\left(\frac{\partial u_i}{\partial x_j} + \frac{\partial u_j}{\partial x_i}\right), \tag{4.1}$$

$$\Omega_{ij} = \frac{1}{2}\left(\frac{\partial u_i}{\partial x_j} - \frac{\partial u_j}{\partial x_i}\right). \tag{4.2}$$

Using the above discussed λ_2 criterion, vortical structures present in the near-wall regions for case A and C are obtained and are shown in figure 4 and 5, respectively. The structures observed in cases B and D are qualitatively similar to those shown in case C below and, therefore, they are not shown.

Figure 4 corresponding to an instant in time of case A shows elongated quasi-streamwise vortices around the near-wall regions, at both the flat channel walls and the wire surface.The presence of streamwise vortices in the near-wall region is analogous to those observed in the wall region of turbulent boundary layers (Rajagopalan & Antonia 1993). The streamwise extent of these vortices is approximately $200 - 300$ wall units. These vortices appear to form an overlapping chain-like structure in the streamwise direction which could be interpreted as the result of mutual interaction between these vortices. The streamwise extent of this chain-like region is about $800 - 900$ wall units. These structures tend to have positive and negative tilt with respect to the axial direction and are inclined at small angles with respect to the vertical direction. Jeong *et al.* (1997) attributes the positive tilt of these structures with positive vorticity, ω_z, and vice-versa. The present observations are consistent with the observed behavior for a turbulent channel flow by Jeong *et al.* (1997).

Figure 5 shows the vortical structures for case C in the near-wall region and the recirculation zone. Away from the recirculation zone, where the flow is attached, quasi-streamwise vortices are observed with features similar to those in turbulent channel flows, boundary layers and case A. The streamwise extent of these vortices is approximately $130 - 300$ wall units. In this region, disorganized vortices near the reattachment zone get distorted (Song & Eaton 2004) owing to mean flow straining and recovery of the boundary layer occurs, thus forming more organized vortical structures (Le *et al.* 1997; Lee & Sung 2002) further downstream of reattachment. Similar to Kaltenbach (2003), downstream of the reattachment zone, densely packed structures exist consisting of entangled filaments with a preferential orientation aligned with the mean flow. Additionally, the complete flow separation from the top of the wire produces a shear layer with intense disorganized vortical structures. In the region of recirculation, the streamwise vortices seem to loose their identity and tend to orient themselves in different direction. This is probably caused by interaction with the axial and cross flows. It also includes effects originating in the three-dimensionality of the shear layer near reattachment (Simpson

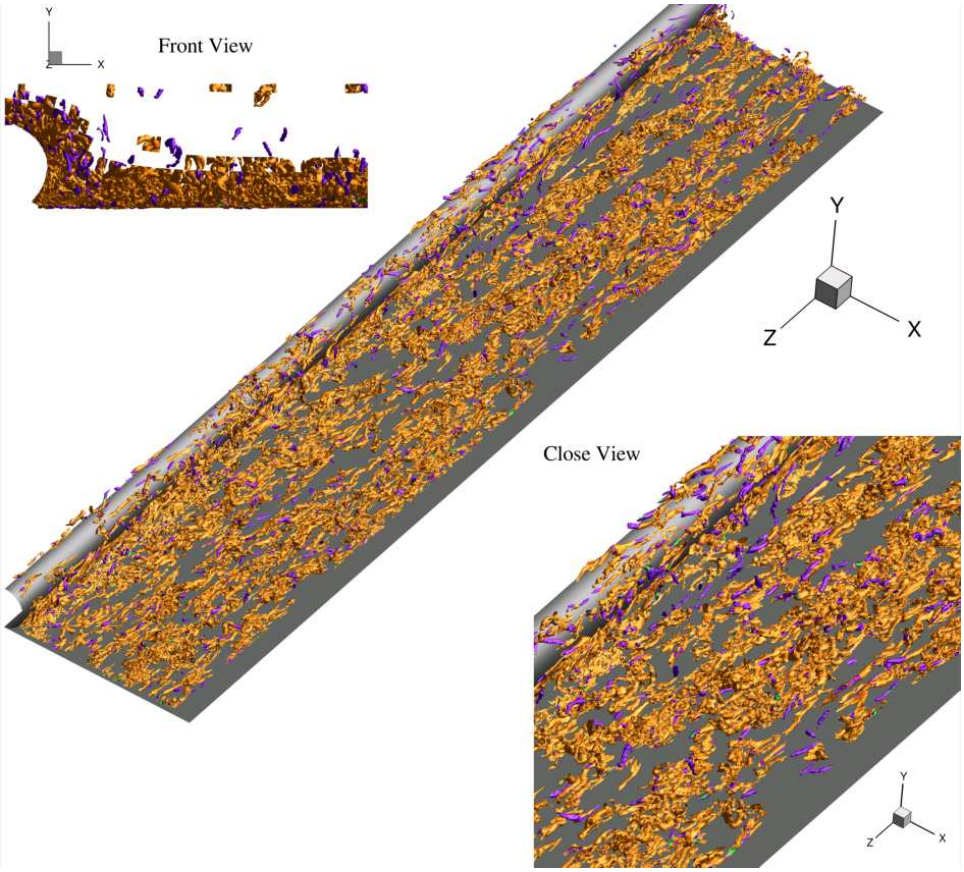

FIGURE 4. Vortical structures in the near-wall region for case A identified by $\lambda_2 = -1$ (orange), $\lambda_2 = -5$ (purple) and $\lambda_2 = -10$ (green).

1996; Mittal *et al.* 2003). Streamwise vortices are also present near the wire top surface with maximum streamwise extent of about 400 wall units. These structures loose their streamwise orientation once the flow detaches to form the shear layer.

The vorticity vector is closely associated with the orientation of the vortical structures as mentioned by Honkan & Andreopoulos (1997). Thus, figure 6 shows the effect of cross flow on the orientation of these vortical structures by inspecting the iso-surfaces of ω_z in the near-wall region and in the shear-layer region. The axial vorticity, ω_z, shows a negative tilt with respect to axial direction in the near-wall region. This is similar to the behavior observed in turbulent channel flow if one considers that the mean flow is oriented at an angle with respect to the z axis, when cross flow is present in the recirculation bubble. This angle is opposite to the mean flow outside the recirculation zone in the attached regions owing to the flow reversal. The vorticity shows both positive and negative tilts with respect to the mean direction of the flow in the recirculation bubble, as expected. However, the vorticity does not show a specific orientation in the shear-layer region. This is a characteristic that is often encounter in free-shear flows. Although the detached shear layer is not, properly speaking, a free-shear flow, in practice, at the Reynolds number of case C, it appears to be very nearly so.

Attempts to identify the qualitative behavior of the vortical structures around the mean reattachment line (to be defined properly below) were mostly unsuccessful. We believe

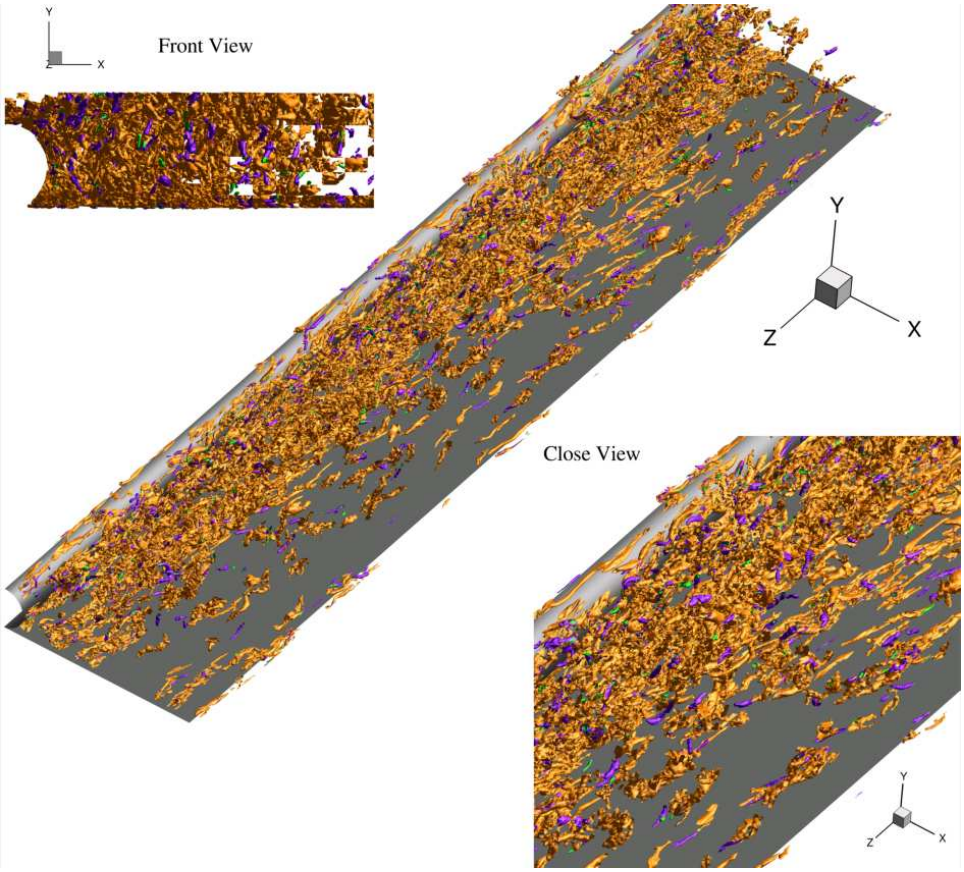

FIGURE 5. Vortical structures in the near-wall and recirculation regions for case C identified by $\lambda_2 = -1$ (orange), $\lambda_2 = -5$ (purple) and $\lambda_2 = -10$ (green).

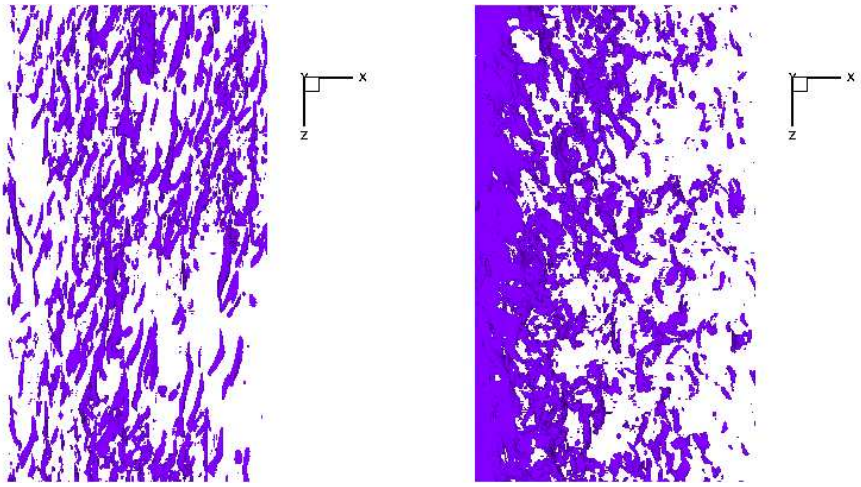

(a) Near wall (b) Shear layer

FIGURE 6. Iso-surface of axial vorticity, $\omega_z = -3$, for case C in the near-wall region with y^+ ranging from 15 to 60 (a) and in the shear-layer region with y^+ ranging from 160 to 370 (b).

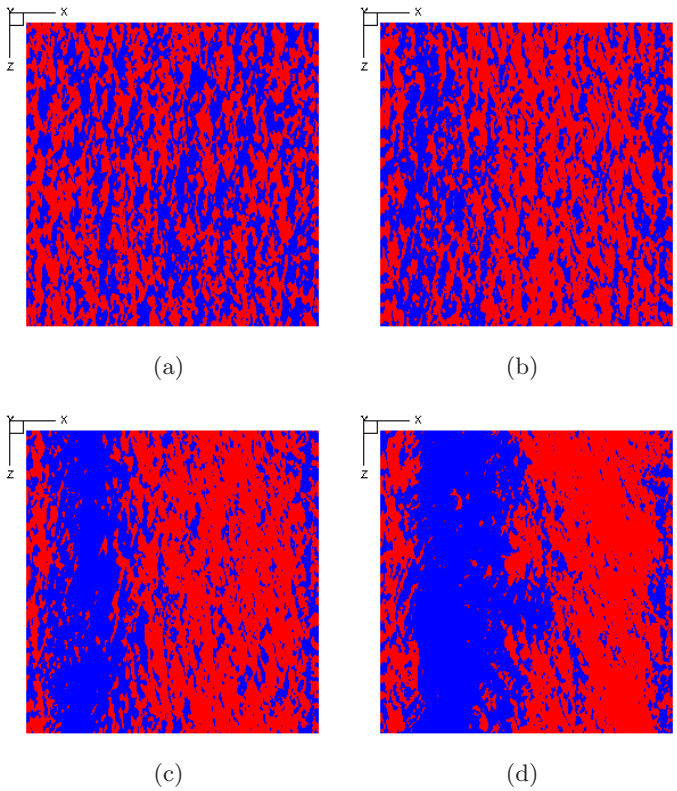

FIGURE 7. Iso-contours of cross flow velocity for cases A (a), B (b), C (c) and D (d) on the $y = 0.05$ plane. Positive and negative values are colored 'red' and 'blue', respectively.

this to be caused by the large contrast in strength of the vortical structures just outside the recirculation bubble with the strength of the structures just inside the bubble. As shown in the previous figures, there is a clear contrast between the structures inside the recirculation bubble and those structures outside, but the distinction is not clear in the intermediate region (where the recirculation bubble reattaches, in the mean). Certainly, the reattachment region only exists in the mean quantities and it is not an instantaneous feature of the flow which may help to explain part of the difficulty associated with identifying any particular structure here. Similarly, no particular type of structure was observed in the secondary recirculation bubbles present within the main recirculation bubble (discussed below). These are even weaker than the main recirculation bubble and are observed primarily in the mean velocity field.

In the present study the reattachment line is defined as the contour of zero cross flow velocity, i.e. the line which separates regions of positive and negative u velocity. The instantaneous separation and reattachment is a highly three-dimensional process as discussed in Na & Moin (1998), where it was shown that the occurrence of a mean reattachment point in a two dimensional bubble is merely a consequence of time averaging. This is apparent in the present study as well. The contours of cross flow velocity for all the cases on a horizontal plane at $y^+ = 15$ is shown in figure 7. It is clear that the reattachment process is highly three dimensional along the axial direction. In case A there is no separation in the mean, however instantaneous negative velocity is observed. In case B, we observe that there is a mean recirculation zone, but the reattachment line

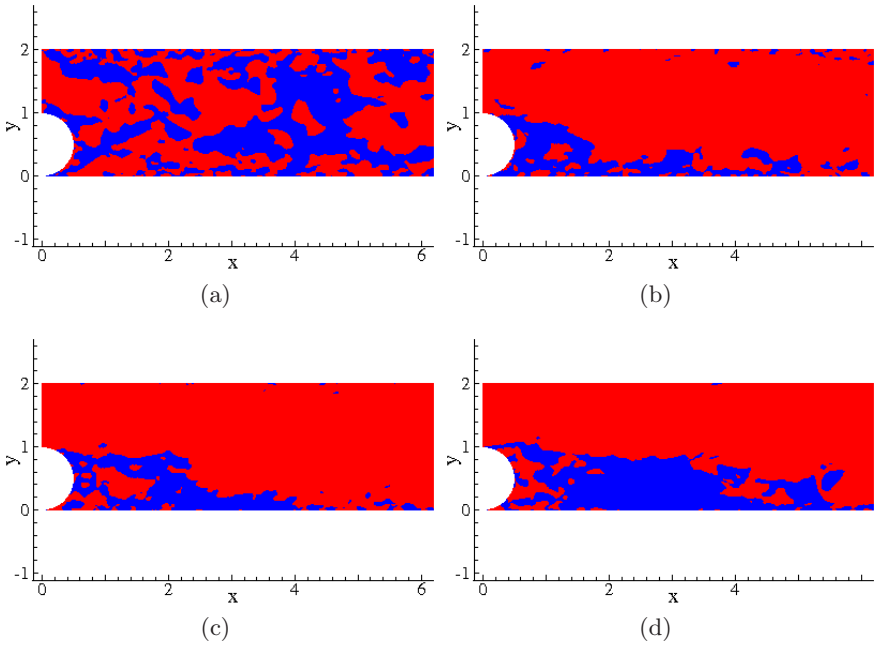

FIGURE 8. Iso-contours of cross flow velocity for cases A (a), B (b), C (c) and D (d) on the $z = 4\pi$ plane. Positive and negative values are colored 'red' and 'blue', respectively.

along the axial direction can not be distinguished. Moreover, in case C and case D, the reattachment process is somewhat more clear, showing an approximate periodic variation superimposed with small scale fluctuations.

To further explore the instantaneous reattachment point, contours of cross-stream velocity are shown in figure 8 on a representative vertical plane located at the center of channel. A similar behavior is observed at other vertical planes (not shown here). The cases with cross flow show instantaneous reversal of the cross-stream velocity. These recirculating regions grows in size with increasing cross flow, although a clear reattachment curve can not be distinguished close to the wall because of the alternating nature of the velocity there. Previous studies of backward-facing step (Simpson 1996; Le *et al.* 1997) and flow over a rib (Liua *et al.* 2008) have attributed the temporal variation of the reattachment zone to the motion of large scale vortices and their interaction with the flapping motion of the separation bubble.

5. Turbulence statistics

The mean velocity profiles are investigated first, both in the unscaled unrotated original coordinates and in the inner-scaled shear stress coordinate frame. This is followed by a discussion of the behavior of turbulence kinetic energy and its corresponding budget terms in the balance equation. Finally, a more detailed discussion of the behavior of the turbulence intensities at particular locations is included.

5.1. *Mean flow*

Iso-contours of the mean axial velocity, $W = \langle w \rangle$, are shown in figure 9 for all cases. In case A, without cross flow, the velocity in the center of the channel is similar to that of a turbulent channel flow. As expected, symmetry is observed about the mid-plane because

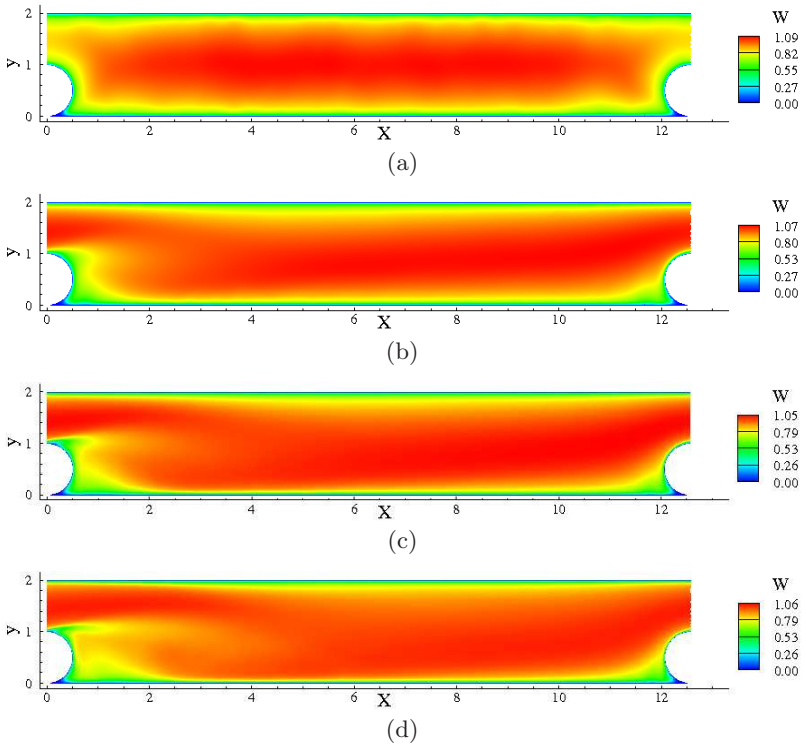

FIGURE 9. Iso-contours of mean axial velocity for cases A (a), B (b), C (c) and D (d).

of the inherent symmetry of the boundary conditions. The effect of the wire is felt up to approximately two wire diameters to each side. In this region, there is a decrease in the vertical velocity gradient near the walls. In the cases with cross flow, a region of detached flow forming a recirculation bubble adjacent to the wire is observed. This detached-flow zone is created by the imposed cross flowrate. The flow separates from the top surface of the wire owing to the large adverse pressure gradient and curvature effects associated with the deceleration of the flow as it approaches the lee-ward side of the wire. In the present case, the cross flow also interacts with the flow in the axial direction. The effect of increasing amount of cross flow is reflected in an increase in the size and a shift in the center of the recirculation bubble. Towards the center of the channel, mean axial velocity contours resemble those of a turbulent channel flow. In the wind-ward side of the wire, a small recirculation bubble close to the wire is observed. The extent of this detached-flow region remains nearly the same in all cases with cross flow.

Iso-contours of the mean cross flow velocity, $U = \langle u \rangle$, and a projection of the mean streamlines in the $x - y$ plane are shown in figure 10. Results for case A are not shown because U is very small in this simulation and there is no recirculation zone. In all other cases, the flow separates as it approaches the top of the wire and forms two clear recirculation bubbles in the lee-ward side of the wire. These bubbles will be referred to as the primary and the secondary bubbles from here onwards. The primary bubble is larger than the secondary bubble, as their naming implies. The size of both bubbles increases with increasing cross flow. The x coordinate of the center of the primary bubble is denoted by x_b and the flow reattaches at the cross flow location x_r. Both x_b and x_r increase with increasing cross flow in the present simulations. High-velocity gradients occurs at the top of the wire and a shear layer is generated. The shear layer is approximately at the

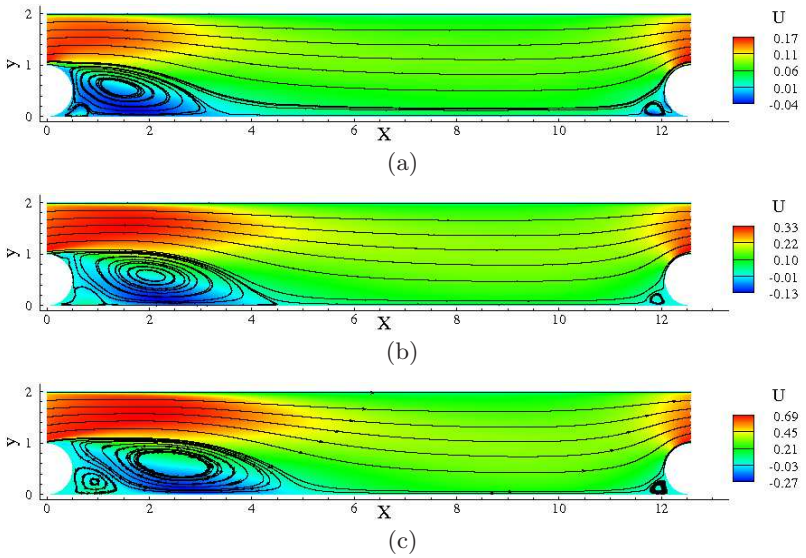

FIGURE 10. Iso-contours of mean cross velocity and two-dimensional projection of the mean streamlines for cases B (a), C (b) and D (c).

boundary between the recirculation bubble and the main cross flow. After reattachment of the primary bubble, the flow recovers towards the center of the channel. When the flow reaches the wind-ward side of the wire, it starts accelerating owing to the reduction in cross sectional area and thus leads to the formation of another secondary recirculation bubble close to the wire. The size of this bubble remains similar in all cross flow cases. The x coordinate of the secondary bubbles, lee- and wind-ward side, are denoted by x_{b2} and x_{b3}, respectively.

Qualitatively, the flow can be classified into four general regions, namely: the recirculation bubbles, the shear layer, the attached flow region in the center of the channel and the acceleration region in the wind-ward side of the wire. In the present simulations, the amount of cross flow is below the threshold required for the appearance of an additional secondary recirculation bubble attached to the top wall of the channel. It is observed in figure 10 that the upper streamlines bend slowly downward but the pressure gradient is insufficient to induce flow separation. For example, such secondary bubble is observed in previous studies on the top wall of flow over backward-facing steps (Armaly *et al.* 1983; Shih & Ho 1994) and on the opposite wall to a constriction in a channel (Mittal *et al.* 2003).

A three-dimensional rendering of selected mean streamlines for case C are shown in figure 11. The figure shows six streamlines in the vicinity of the wire where the recirculation zone is observed. The streamlines s_1 and s_2 emanate from regions above the primary bubble. These streamlines skip the bubble region and travel towards the attached flow region. The streamlines s_3, s_4, s_5 and s_6 are located within the primary bubble region. The rotational character of the flow is observed in these streamlines, where the spiraling behavior is indicative of the presence of axial flow. It can be observed that streamlines s_3 and s_4 make one complete rotation about the axial direction, while streamlines s_5 and s_6 have achieved approximately half a rotation. This type of spiral or helical path has been observed previously, for example by Kaltenbach & Janke (2000) in a study of flow behind a swept rearward facing step and by Sheu & Rani (2006) in flow over a backward-facing step with side walls.

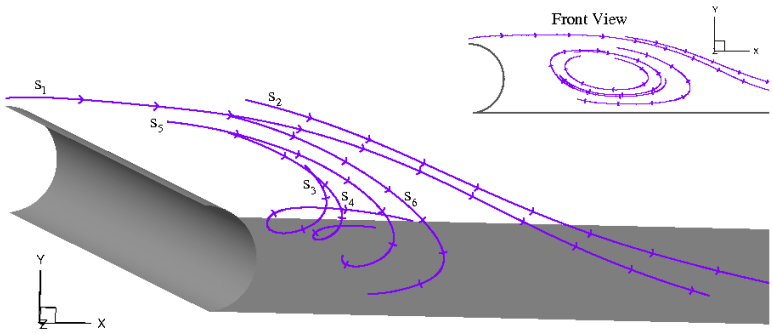

FIGURE 11. Three-dimensional rendering of selected mean streamlines for case C.

Case	Spanwise locations			
	x_t	x_c	x_b	x_r
A	0	2π	-	-
B	0	2π	1.39	3.29
C	0	2π	2.01	4.65
D	0	2π	2.46	5.34

TABLE 2. Location of observation points along cross flow direction.

Case	Flow Quantity	Spanwise locations			
		x_t	x_c	x_b	x_r
A	u_{τ_b}	0.050	0.055	-	-
	u_{τ_t}	0.049	0.054	-	-
B	u_{τ_b}	0.051	0.057	0.050	0.056
	u_{τ_t}	0.057	0.050	0.056	0.052
C	u_{τ_b}	0.050	0.054	0.053	0.056
	u_{τ_t}	0.059	0.053	0.058	0.055
D	u_{τ_b}	0.050	0.060	0.057	0.064
	u_{τ_t}	0.068	0.060	0.057	0.058

TABLE 3. Friction velocity at different cross flow locations. Subscripts b and t denote values at bottom and top wall, respectively.

The velocity statistics in terms of friction-based, inner, coordinates along the vertical direction, y, at different cross flow locations is investigated next. The profiles are extracted at the locations denoted by x_t, x_c, x_b and x_r, corresponding to the top of the wire, center of the channel, center of primary recirculation zone and reattachment point, respectively. Only the locations x_t and x_c are considered for case A, since it has no recirculation zone. The cross flow locations for all simulations are summarized in Table 2. The profiles of mean velocity component V_s (in the wall shear-stress frame) normalized by the friction velocity, $V_s^+ = V_s/u_\tau$, are shown along the vertical direction in figure 12 as a function of the inner coordinate $y^+ = yu_\tau/\nu$. These profiles have been extracted at each of the planes indicated previously and are shown with respect to the bottom and top wall

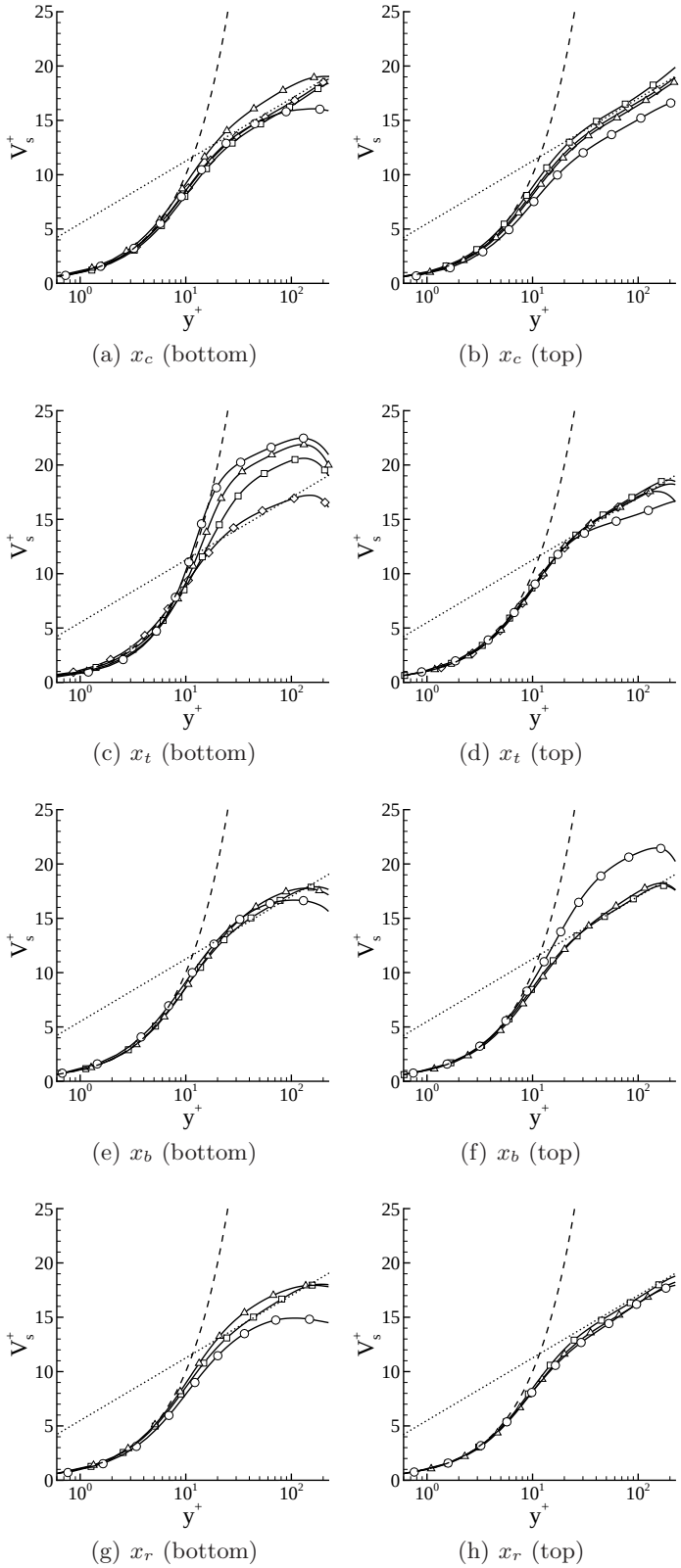

(a) x_c (bottom) (b) x_c (top)

(c) x_t (bottom) (d) x_t (top)

(e) x_b (bottom) (f) x_b (top)

(g) x_r (bottom) (h) x_r (top)

FIGURE 12. Profiles of mean velocity normalized with the friction velocity at different cross flow locations. Case A, B, C and D are denoted with $\diamond$, $\square$, Δ and $\circ$, respectively. Left and right subfigures show profiles from the bottom and top walls, respectively.

distance. The values of friction velocity, u_τ, at the bottom and top walls at different cross flow locations are shown in Table 3 for all the cases. Figure 12 also shows a "Law of the Wall" composed of a viscous sublayer and the logarithmic law for a zero pressure gradient (ZPG) boundary layer with values of the Kármán constant of 0.4 and slope intercept of 5.5. In the present study, the complexity of the flow is such that we did not attempt to incorporate pressure-gradient effects into a reference "Law of the Wall" valid at each location (Nickels 2004), primarily because it is not a priori expected that equilibrium will be reached within the turbulent flow as it travels over the wire surface for such a law to be generally applicable here. Therefore, as a means to establish a reference in the discussion of the profiles, the ZPG law will be referenced but we bare in mind that there is no generally valid reason indicating that the different profiles should necessarily agree with the ZPG law across the channel. The main interest of the following discussion is to investigate whether the inner-scaled velocity obeys a "Law of the Wall", i.e. $V_s/u_\tau = F(y^+)$, and in the cases where it does, up to what distance above the wall is this approximation appropriate. This is motivated by practical needs to develop wall closure models in complex flows, e.g. wall-shear-stress models (Schumann 1975).

Figures 12(a) and (b) show the velocity profiles at location x_c, center of the channel, from the bottom and top walls, respectively. All profiles, except at the highest cross flowrate, show good agreement with the ZPG law when measured with respect to the bottom and top walls. The observed increasing deviations with increasing cross flowrate are caused by the growth of the main recirculation bubble. At the fixed x_c, the reattachment point of the recirculation bubble is closer as the cross flowrate increases, implying increasing non-equilibrium effects, i.e. larger recovery distance from the reattachment point and persistence of large scale vortices (Eaton & Johnston 1981; Simpson 1996; Le *et al.* 1997; Na & Moin 1998; Spalart & Strelets 2000; Liua *et al.* 2008). Figures 12(c) and (d) show the profiles at location x_t, top of the wire, measured from the bottom and top walls, respectively. Significant deviation from the ZPG in the inertial sublayer is observed on the top of the wire. The profile of case A, without cross flow, follows the viscous sublayer and logarithmic law reasonably well. The cases with cross flow deviate from the logarithmic law and exhibit higher values in this region but remain remarkably parallel to the logarithmic law; most of the deviation is therefore with respect to the slope intercept value. This is likely caused by the strong streamline curvature effects induced by the wire and favorable pressure gradient (FPG) present on the upstream side (Webster *et al.* 1996). The profiles for all cases but case D measured from the top wall follow the ZPG law. The profile for case D shows a lower slope with respect to the ZPG law with increasing distance in the intermediate subrange. This behavior can not be modeled only by adjusting the slope intercept value since the Kármán constant appears to change; provided a logarithmic law is assumed. Figures 12(e) and (f) show the profiles at location x_b, the center of the main recirculation bubble, measured from the bottom and top walls, respectively. The profiles from the bottom wall exceed the ZPG law by a small amount. In particular, the profiles of the cases with cross flow in the inertial sublayer do not appear to be parallel to ZPG profile and a continuous bending of the profiles is observed. The profiles measured from the top wall for all, but case D, collapse approximately with the ZPG. The profile for case D from the top wall exceeds the ZPG law by a large amount, indicating that the flow is subjected to substantial FPG. Thus, at location x_b, which is located under the recirculation bubble, the logarithmic-region of the ZPG profile is approximately followed in all cases, except for the top wall profile of the simulation with the largest cross flow. In previous studies of backward facing steps and similar flows, the velocity profile in the separation bubble does not exhibit a logarithmic range owing to adverse pressure gradients (APG) (Dianat & Castro 1991; Kiel & Vieth

1995; Le *et al.* 1997; Na & Moin 1998; Simpson 1996; Spalart & Strelets 2000; Angele & Muhammad-Klingmann 2006). In the present case, there is an imposed axial flow, large swept angle, and there is dominant turbulent wall-bounded flow in the z direction. Only in case D, with the highest cross flow and lowest swept angle, an approximate equilibrium turbulence scaling is not observed in the top-wall profile. Note that one should not conclude that there are no pressure-gradient effects on profiles from the top wall just above the recirculation bubble. The difference observed in case D on the top wall, with respect to the ZPG law, is caused by the fact that FPG is still present at x_b. Similar FPG-like scaling is observed to the left of x_b in the other simulations with cross flow, e.g. see figure 13 and associated discussion. In case D, the FPG extends well over the recirculation bubble and affects the observed scaling there. Finally, figures 12(g) and (h) show the profiles at location x_r, where the flow reattaches, measured from the bottom and top walls, respectively. At this location, there is substantial deviation of the bottom-wall profiles with respect to the ZPG for simulations C and D. The profiles for case B collapses with the ZPG profile. The profiles of cases C and D have values higher and lower than those predicted by the ZPG law, respectively. Near the reattachment zone, the flow is far from equilibrium owing to the presence of large scale vortices (Kiya & Sasaki 1985) and impingement of vortical structures on the wall (Shih & Ho 1994; Simpson 1996; Na & Moin 1998; Kaltenbach 2003; Dejoan & Leschziner 2004; Hudy *et al.* 2007). The profiles measured from the top wall for case B collapse again and differ slightly from that of case C and D, where lower values are observed in inertial sublayer, indicative of APG.

Overall, these results indicate that the cross flow in case D is substantial and this has a major impact on the inner-scaled velocity at different locations. In this case, the axial flow may not be strong enough to provide a dominant source of turbulence fluctuations; the flow is approaching the behavior of backward-facing step flows. Moreover, bottom and top wall show more deviation of the mean velocity from the ZPG law in the logarithmic regions. This can be attributed to significant pressure gradient variations in the regions above the primary separation bubble. Excluding the reattachment zone, it appears that a generic "Law of the wall" composed of a viscous and logarithmic sublayers, the latter with pressure-gradient dependent Kármán and intercept constants, is able to parameterize the behavior of the average velocity with respect to the normal coordinate up to approximately $y^+ \sim 100$. This upper limit of is certainly dependent on the Reynolds number, which is moderate in the present simulations. Alternatively, the composite pressure-gradient-dependent formulas proposed by Nickels (2004) could be used. To clarify the behavior of the pressure, variation of pressure gradient in the net mean flow direction is studied for case C.

The mean pressure gradient in the net flow direction defined by the shear-stress coordinate system is given by

$$\frac{\partial \langle p \rangle}{\partial s} = \boldsymbol{\nabla} \langle p \rangle \cdot \vec{s}, \tag{5.1}$$

where $\langle p \rangle$ is the mean pressure and $\vec{s}$ is the net mean flow direction, i.e. in the θ direction. The profiles of $\frac{\partial \langle p \rangle}{\partial s}$ are shown in figure 13 along all surfaces for case C. On the bottom wall, three regions of FPG (negative $\frac{\partial \langle p \rangle}{\partial s}$) are observed, which indicates the primary and two secondary separated-flow regions. After the reattachment point, the pressure gradient shows a linear increase and it becomes APG (positive $\frac{\partial \langle p \rangle}{\partial s}$) until the flow reaches the vicinity of the wind-ward side of the wire. On the top wall, one region of FPG is observed above the wire; note that the region is split in the middle by the periodic boundary. A strong APG region develops before the reattachment point, which is substantially reduces as the flow approaches the center of the channel. These two profiles indicates

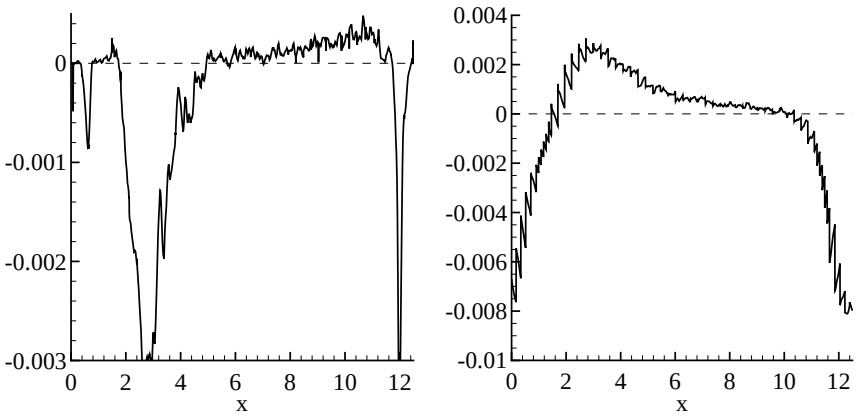

(a) bottom wall (b) top wall

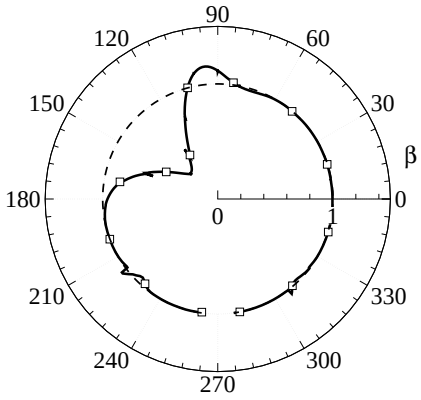

(c) wire surface

FIGURE 13. Pressure gradient along the net mean flow direction for case C on bottom (a) and top (b) walls and on the wire surface (c). Dotted line indicates ZPG.

that equilibrium is not achieved even though the flow is attached in the central portion of channel. On the wind-ward surface of the wire, figure 13(c), a large FPG is observed as the flow accelerates to overcome the are reduction caused by the wire. The pressure gradient reverses just before reaching the top-most point of the wire. Obviously, the flow can not sustain that APG for long and it separates quickly generating a shear layer, which can be seen qualitatively by the sudden drop of the pressure gradient at $\beta \approx 85^o$. After separation, the pressure gradient is minimal on the lee-ward side of the wire. These results complement and are necessary in order to rationalize the observed behavior of the inner-scaled velocity profiles discussed previously.

5.2. *Turbulence kinetic energy and budgets*

Contours of turbulence kinetic energy, $k = 1/2\langle u_i^{'} u_i^{'} \rangle$ in the $x - y$ plane are shown in figure 14. In case A, the peak of k is about 0.015 and it is observed close to the walls and wire surface and it reaches a minimum value towards the center of the channel. The zone around the contact point of the wire with the walls of the channel do not experience the same level of turbulence kinetic energy as that observed in the less confined regions of the flow. The proximity of the walls blocks the development of velocity fluctuations there. In

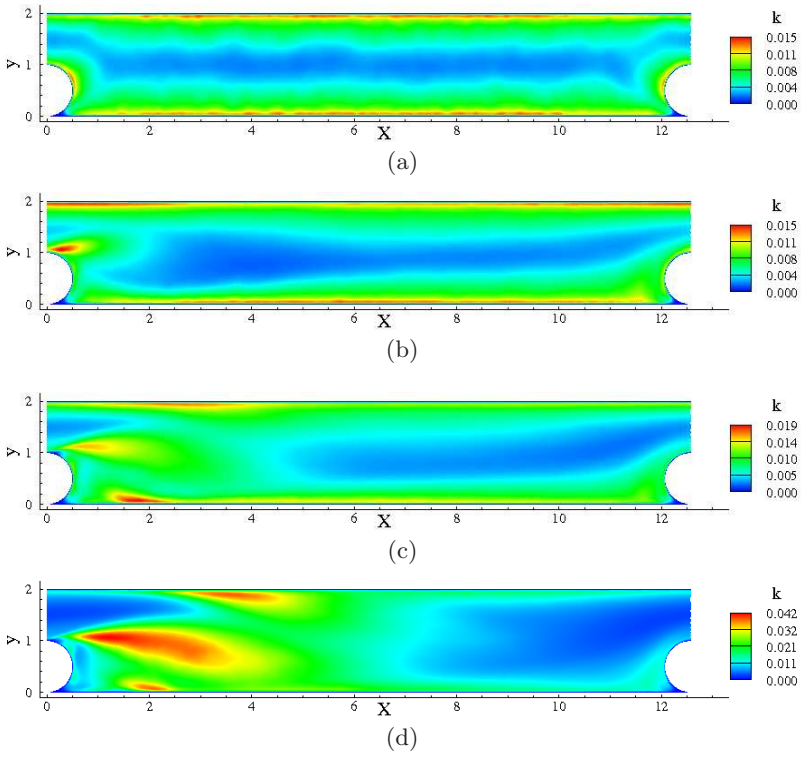

FIGURE 14. Turbulence kinetic energy for cases A (a), B (b), C (c) and D (d).

case B, the peak of k is about 0.015 and it is observed close to the walls, wire surface and shear layer. In the primary recirculation zone, k attains a value of about 0.01. After the flow reattaches, the contours are similar to those of case A, with lower values observed towards the middle of the channel. In case C, the maximum k is about 0.020 and it is observed close to the wall within the recirculation bubble. The turbulence kinetic energy attains higher values near the region of separation and recirculation in comparison to other parts of the channel but there are two lower peaks of k, one at the shear layer and another close to the top wall of the channel in the neighborhood of the wire. In case D, the peak of k is about 0.042 and it is qualitatively similar to case C. However, the regions of large k have grown in size and in magnitude. Lower values of k are observed in other parts of the channel. Part of the increase in kinetic energy is directly associated with the presence of the additional cross flow. This additional flow increases the overall Reynolds number, Eq. (3.11), and one would expect higher levels of kinetic energy as a direct consequence of the increase in the flow rate. Nevertheless, there is now additional production at specific locations owing to the interaction with the axial flow.

The budget equation for the turbulence kinetic energy, k, is given by

$$\frac{\partial}{\partial t}k + \underbrace{\langle u_j\rangle \frac{\partial}{\partial x_j}k}_{\text{convection}} = \underbrace{-\langle u_i^{'}u_j^{'}\rangle \frac{\partial \langle u_i\rangle}{\partial x_j}}_{\text{production}} \underbrace{-\nu\left\langle \frac{\partial u_i^{'}}{\partial x_j}\frac{\partial u_i^{'}}{\partial x_j}\right\rangle}_{\text{dissipation}}$$
$$\underbrace{-\frac{1}{2}\frac{\partial}{\partial x_j}\langle u_i^{'}u_i^{'}u_j^{'}\rangle}_{\text{turbulent transport}} + \underbrace{\nu\frac{\partial^2}{\partial x_j \partial x_j}k}_{\text{viscous diffusion}} - \underbrace{\frac{1}{\rho}\frac{\partial}{\partial x_i}\langle u_i^{'}p^{'}\rangle}_{\text{pressure transport}}, \qquad (5.2)$$

where, P, T, ϵ, π, D and C denotes turbulence production, transport, dissipation, pressure transport, viscous diffusion and convection, respectively. The profiles of the terms P, T, ϵ, π, D and C throughout the span of the channel are obtained at location x_c for case A and at location x_b for the remaining cases. These profiles are shown in figure 15. The location x_b is important as it covers the shear layer region. In case A, the peaks of all the budget terms are located near the top and the bottom wall. Towards the center of the channel, all the budget terms becomes insignificant because in this region the turbulence kinetic energy is small. In the cases with cross flow, peaks are also observed near both walls and towards the center of the channel, where the shear layer is located. The value of the local peaks of these quantities increases with increasing cross flow. This increase is clearly observed in case C and case D. In the latter case, in the shear layer and recirculation bubble, T becomes a dominant source of turbulent energy production mechanism and balances dissipation. This is consistent with reported results for a separated turbulent boundary layer by Dianat & Castro (1991). The production term P, becomes negative in this region which indicates strong deviation from equilibrium conditions as mentioned by Kaltenbach (2003). Above the shear layer zone, it is observed that turbulent transport in conjunction with convection becomes a source of turbulence kinetic energy. Near the wall, dissipation is balanced by viscous diffusion (Na & Moin 1998).

5.3. *Turbulence intensities*

One difficulty that must be considered when analyzing the overall behavior of statistical profiles as a function of y across the channel height is the impossibility of defining a unique flow direction valid over the extent of the channel. According to our previous parametrization, section 3.3, it is possible to define at least three different directions at any particular value of x. These are the two directions determined from the local mean wall shear stress, similar to Eq. (3.7), as well as a direction defined by the local average flow rate through this plane. The latter being analogous to the angle defined from Q_x and Q_z, appropriately rescaled. One immediately realizes that none of these angles provides a clear and unique direction at a particular station because the flow is not homogeneous in the x direction. Therefore, we chose to discuss the turbulence intensities in the frame of the simulation and avoid rotating the velocity components in any particular direction to prevent introducing an additional degree of arbitrariness.

The profiles of turbulence intensities, i.e. the root mean square (r.m.s.) velocity fluctuation, normalized by friction velocity at different cross flow locations, x_t, x_c, x_b and x_r, are shown in figure 16, 17, 18 and 19, respectively. The quantities u_{rms}, v_{rms} and w_{rms} denote cross flow, vertical and streamwise intensity, respectively. Comparison of the turbulence intensities for case A between figure 16(a) and figure 17(a) show that u_{rms} is larger than v_{rms} at around $y = 1.5h$, in contrast with the profiles at x_c where in the middle of the channel both take the same value. In the cases with cross flow, the largest

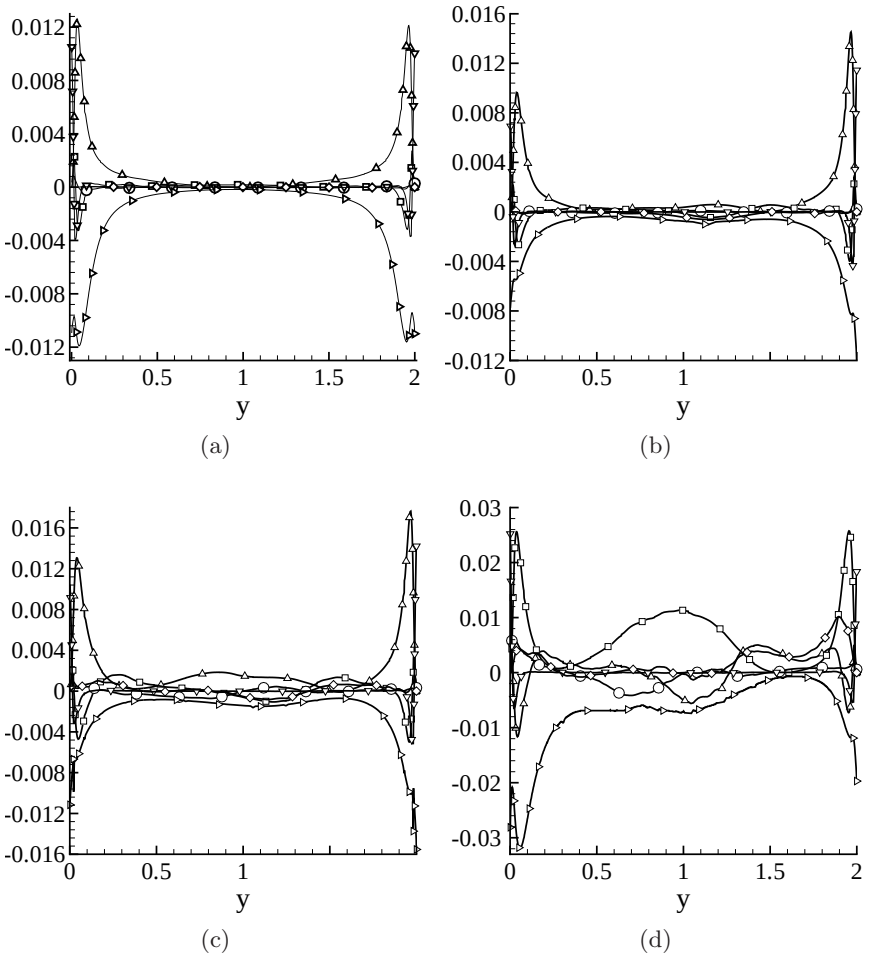

FIGURE 15. Profiles of turbulence kinetic energy budget terms at location x_c for case A (a) and at location x_b for case B (b) and C (c) and D (d). P, T, π, D, C and ϵ are denoted by Δ, $\Box$, $\circ$, $\triangledown$, $\diamond$ and $\triangleright$, respectively.

change is observed in the values of w_{rms}, which has a peak that now attains a maximum value close to the top wall of the channel. The peak closer to the top of the wire is lower than that close to the top wall. As the cross flow increases the relative values of the intensities change owing to the change in the mean direction of the flow. The value of w_{rms} in case A is observed to be slightly lower in the near wall region and slightly higher in the outer part of the boundary layer than those of a flat plate boundary layer. This is consistent with the study of Snarski & Lueptow (1995) of a turbulent boundary layer on a cylindrical surface, where the difference was attributed to low surface area near the wall and less constraints in the outer region of the flow.

The profiles at x_c for case A look approximately symmetric about the center of the channel and they are similar to those of a turbulent channel (Kim *et al.* 1987). This is because there is no separation of the flow in case A and the effect of the wire is not significant towards the central region of the channel. In case B, the profiles start to lose symmetry, indicating recovery of the flow in this region is not yet complete. The value of u_{rms} is higher than v_{rms} in most of the channel except at the center, where they take

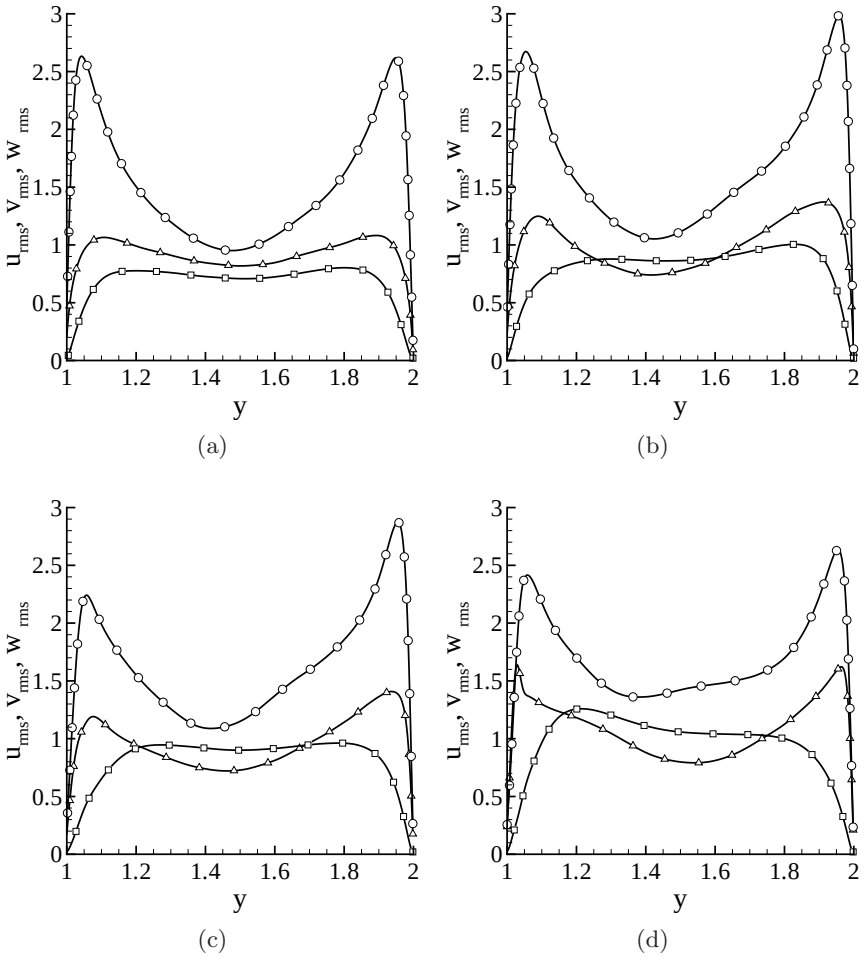

FIGURE 16. R.m.s. velocity fluctuations normalized by friction velocity at location x_t. The different intensities are u_{rms} (Δ), v_{rms} ($\square$) and w_{rms} ($\circ$). Subfigures denote cases A (a), B (b), C (c) and D (d).

similar values. In case C and D, where the amount of cross flow is higher, the profiles loose their symmetry and the minimum value does not occur at the center of the channel. The location of minimum turbulence intensity is observed towards the lower half of the channel. In both of these cases, away from the wall, the u_{rms} and v_{rms} profiles do not vary significantly. In case D, the value of u_{rms} increases in most of the channel and it is associated with high turbulence kinetic energy in the outer part of the boundary layer (Johnston 1970).

The profiles at x_b in all the cases with cross flow look very different compared to the profiles at the previous locations. All the profiles develop a peak in turbulence intensity, all components, towards the center of the channel. This is a manifestation of the presence of the shear layer. In case B, the highest peak of w_{rms} occurs towards the top wall of the channel while in the higher cross flow cases it occurs towards the bottom wall of the channel. The maximum value of w_{rms} is higher for case C and D compared to case B. In case D, the peak value of u_{rms} is close to w_{rms} near the walls and in the regions of recirculation u_{rms} attains higher values compared to w_{rms}. The value of v_{rms} is higher in

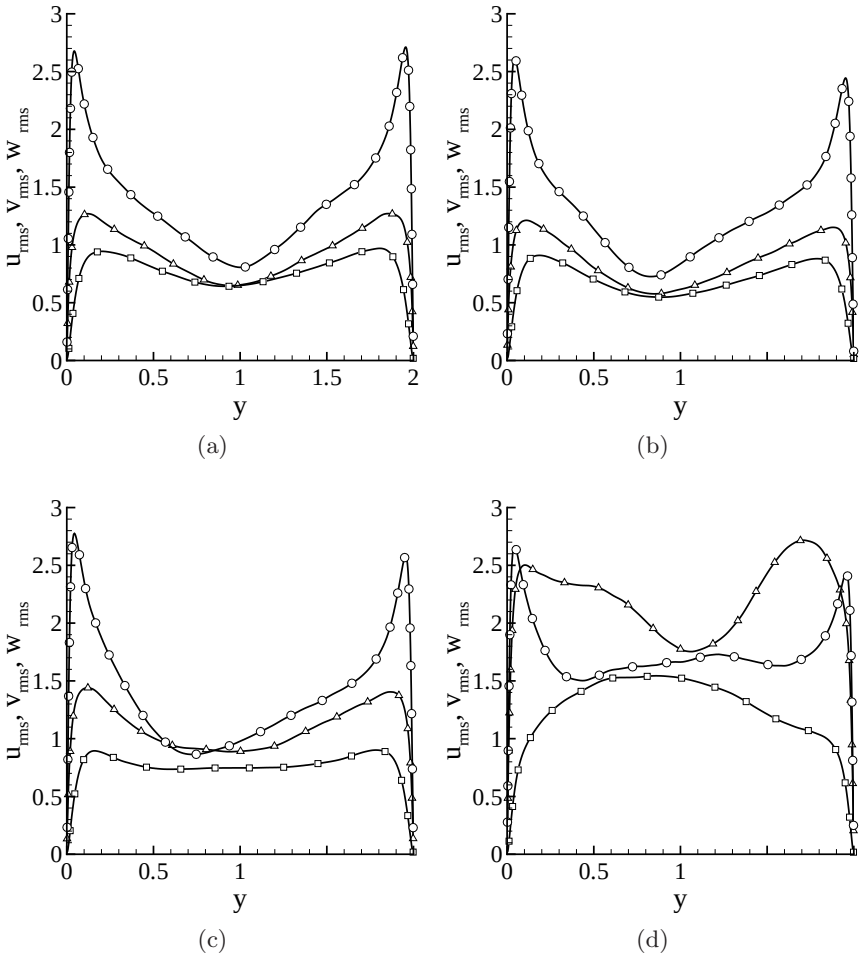

FIGURE 17. R.m.s. velocity fluctuations normalized by friction velocity at location x_c. The different intensities are u_{rms} (Δ), v_{rms} ($\square$) and w_{rms} ($\circ$). Subfigures denote cases A (a), B (b), C (c) and D (d).

the region with recirculation. The maximum value of v_{rms} increases with increasing cross flow. In case B, the maximum value is close to the streamwise intensity while in case C and D the maximum value is even higher than the streamwise and cross flow maximum values. In the lower half of the channel the values of vertical intensity is higher compared to other intensities. This is similar to high turbulence intensity observed in shear layers in earlier studies of separating/reattaching flows (Eaton & Johnston 1981; Shih & Ho 1994; Liua *et al.* 2008). Kaltenbach & Janke (2000) have attributed such increase of turbulence intensity in the shear layer of a swept flow to the extensional strain of vortical structures present in the shear layer.

The profiles at x_r, where the mean flow reattaches to the wall, are similar to those of a turbulent channel for cases B and C, with peak values near the wall and the presence of a local minimum towards the center. However, in case D, the profile shows substantial variation. The maximum value of of u_{rms} increases as the amount of cross flow is increased. The value of v_{rms} is highest near the walls and shows less variation towards the center of the channel, increasing with increasing cross flow. This region shows that

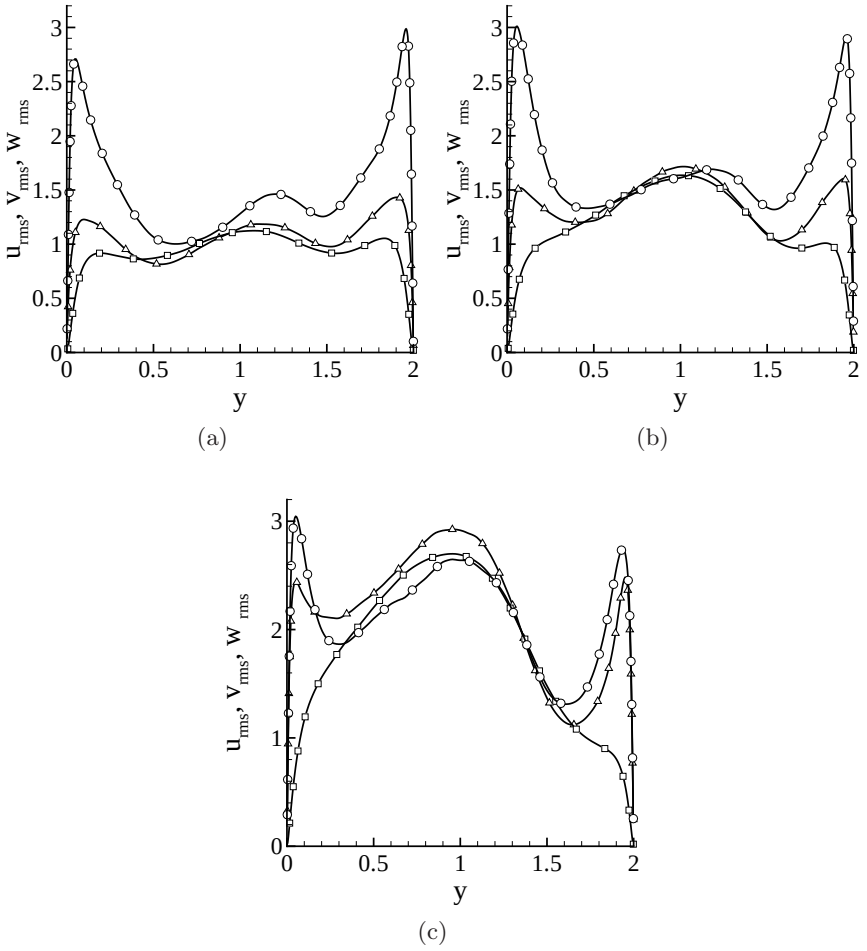

FIGURE 18. R.m.s. velocity fluctuations normalized by friction velocity at location x_b. The different intensities are u_{rms} (Δ), v_{rms} ($\square$) and w_{rms} ($\circ$). Subfigures denote cases B (a), C (b) and D (c).

decay of turbulence intensity starts to occur near the reattachment region. This decays is more apparent in case B and C, compared to case D.

6. Statistics of the recirculation bubble

The type of reattachment observed in the present simulations was termed as being of ordinary type by Johnston (1970) in a study of swept forward-facing step. In this case, the wall shear stress is not zero at the reattachment point. The observed reattachment length in the simulations increases with increasing Re; similar to findings over backward-facing steps (Armaly *et al.* 1983; Adams & Johnston 1988; Li & Naguib 2005). The shear layer created at the top of the wire separates the recirculation bubble, which is characterized by the presence vortical structures (Chun & Sung 2003; Song & Eaton 2004). The intensity of the turbulence kinetic energy is large, as discussed earlier. The locus of the peak of k in the shear layer along with the mean dividing streamline and iso-contours of k for case C are shown in figure 20. The locus of peak turbulence kinetic

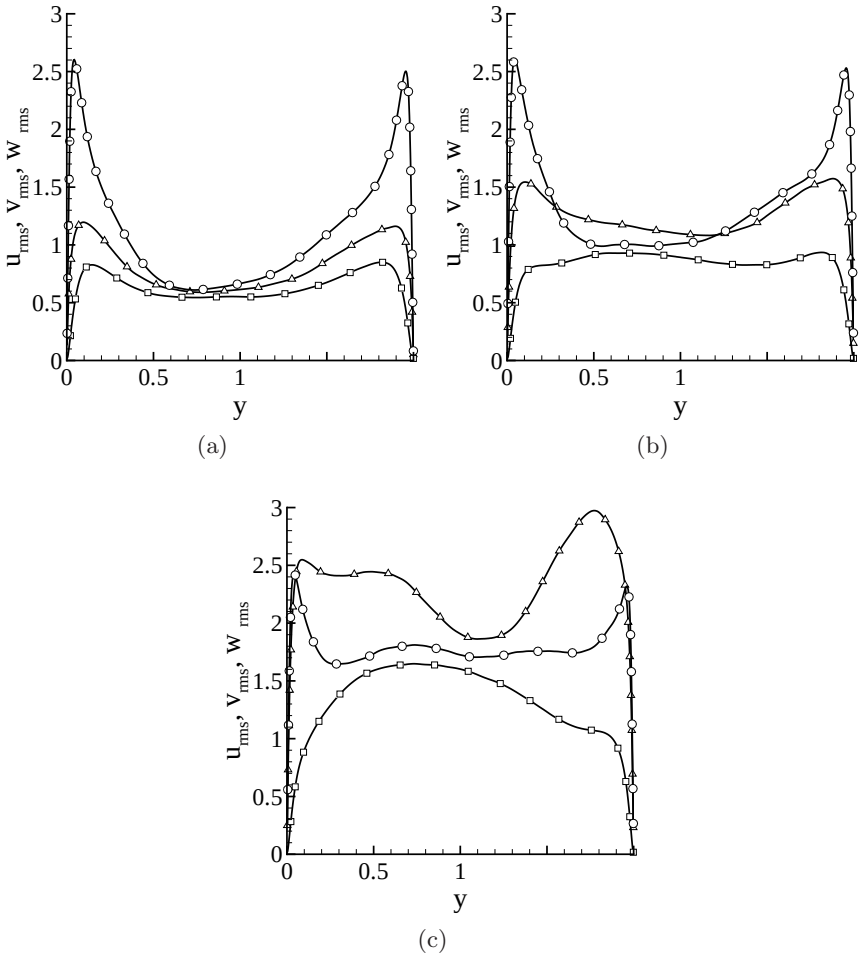

FIGURE 19. R.m.s. velocity fluctuations normalized by friction velocity at location x_r. The different intensities are u_{rms} (Δ), v_{rms} ($\square$) and w_{rms} ($\circ$). Subfigures denote cases B (a), C (b) and D (c).

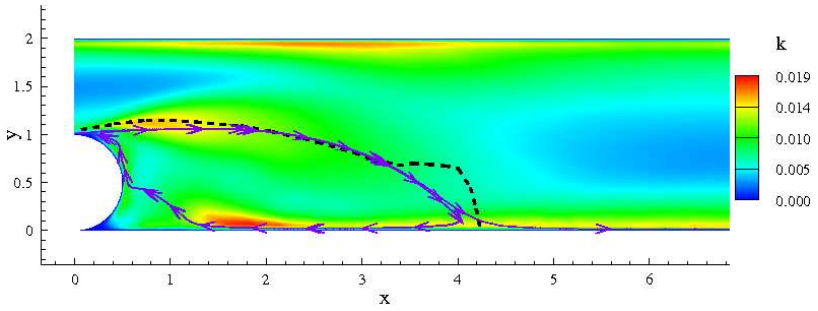

FIGURE 20. Iso-contours of turbulence kinetic energy overlayed with mean streamlines (solid curves with arrows) and locus of maximum kinetic energy (dotted curve) in the shear layer for case C.

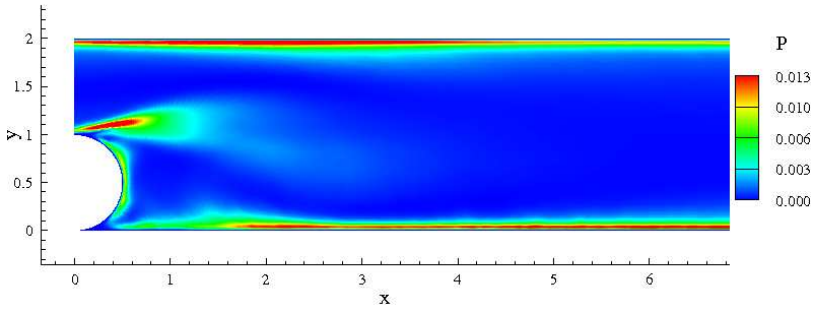

(a)

FIGURE 21. Iso-contours of production of turbulence kinetic energy for case C.

energy is usually used as an approximation for the center of the shear layer (Dianat & Castro 1991). At the separation point, this curve deviates from the mean dividing streamline but shortly after it follows the mean dividing streamline over most of the primary recirculation zone. Further deviation of the peak turbulence kinetic energy locus and the mean dividing streamline is observed before reattachment. This would suggest that the outer regions near reattachment still contains high values of turbulent intensity and there is a spill of large scale vortical structures; similar to that observed in backward-facing step flow (Eaton & Johnston 1981). A complementary study of the behavior of this shear layer focuses on the fluid entrainment (Liu *et al.* 2007, 2006; Li & Naguib 2005) and its association with the reattachment length.

An important difference between the present flows and previous studies is that a large fraction of the primary bubble is in a fully turbulent state; caused by the large axial flow. Iso-contours of turbulent production, P, are shown in figure 21 for case C. It is observed that P is high close to the separation point and formation of the shear layer as well as close to the wall within the recirculation zone. The levels of turbulence production in the vicinity of the wall is similar within the recirculation region and the fully attached flow. This indicates that the separated bubble is characterized by the presence of a strong turbulent boundary layer. The strength of the turbulence kinetic energy and production term in the shear layer zone are substantially reduced half-way to reattachment. There is a rapid decay of the vortical structures before impingement on wall. These features are substantially different from other separated/reattached flows where the flow within the recirculation bubble has features of a laminar boundary layer (Dianat & Castro 1991). The turbulence kinetic energy and production have much smaller value under the secondary, smaller, recirculation bubble close to the wire. Figure 20 shows that the turbulence kinetic energy is large just before the secondary separation leading to the formation of the secondary recirculation bubble. This flow resembles, to some extent, to separation induced in flat turbulent boundary layer by an imposed adverse pressure gradient. The APG can be seen in figure 13(a) at approximately $x = 1.5$, which is close to the location of the flow separation observed in figures 20 and 21.

Finally, the turbulence energy spectra for case C at four locations are shown in figure 22. A reference line corresponding to $-5/3$ power-law is also shown in the plots to compare with inertial subrange Kolmogorov scaling. The locations shown corresponds to the center of the shear layer, center of the bubble, near reattachment location inside the bubble and at the center of the channel. The x, y and y^+ coordinates of these locations are provided in Table 4. The inner coordinate y^+ is measured from bottom wall. It is observed that in the intermediate wave number range, the energy decay may approximate

Location	x	y	y^+
Shear layer	2.17	1.04	324
Center of bubble	2.01	0.58	181
Near reattachment	3.61	0.17	53
Center of channel	6.31	1.00	312

TABLE 4. Coordinates of the locations where turbulence energy spectra is obtained.

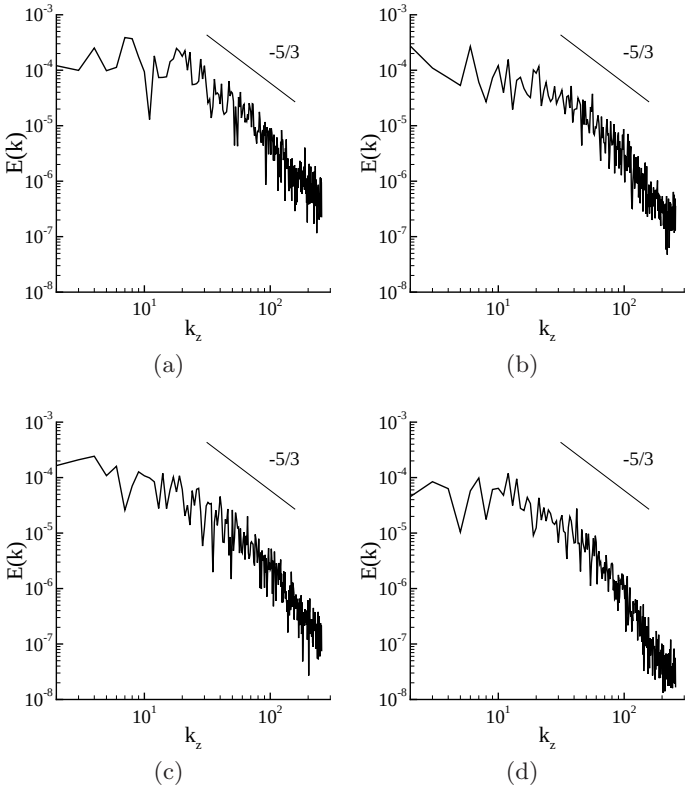

FIGURE 22. Energy spectra for case C at four different cross flow locations, shear layer (a), center of recirculating bubble (b), near reattachment location (c) and center of channel (d).

the $-5/3$ power-law, although the Reynolds number may not be sufficiently large for an inertial subrange to be clearly defined. Nevertheless, the level of turbulence kinetic energy and the shape of the spectra clearly indicates that the flow is fully turbulent within a large fraction of the primary recirculation bubble.

7. Shear stress distribution

It is well recognized that measurements of wall shear stress is a difficult and critical task owing to the experimental uncertainties involved (Honkan & Andreopoulos 1997). This is an important physical quantity which is useful for both modeling as well as in applications. Moreover, it is used to determine inner scaling of the velocity profiles as well as skin friction. Therefore, the statistics of the instantaneous shear-stress on the bottom wall and the wire surface are investigated here. The shear stress, τ_{ij}, is defined

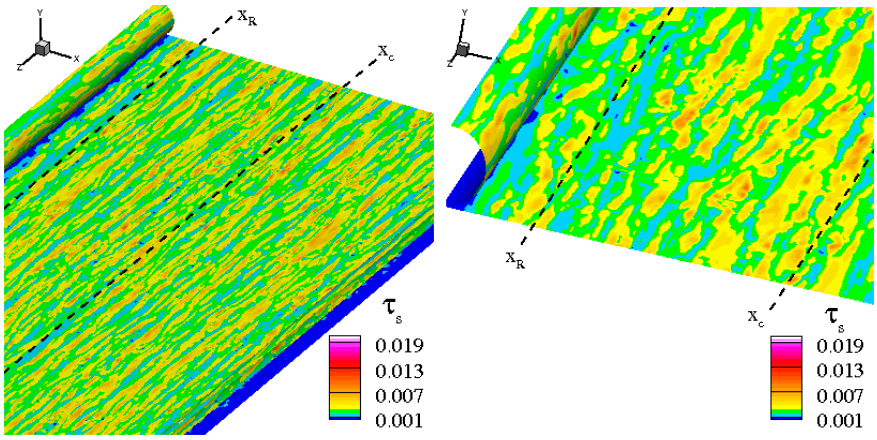

(a) (b)

FIGURE 23. Iso-contours of friction stress, τ_w, on the bottom wall including the wire surface for case A. Subfigure (a) contains a large scale view of the wall shear stress while subfigure (b) shows a zoom on the indicated region.

as,

$$\tau_{ij} = \mu \left(\frac{\partial u_i}{\partial x_j} + \frac{\partial u_j}{\partial x_i} \right), \tag{7.1}$$

where μ is the dynamic viscosity and u_i is velocity component. The traction T_i, caused by shear stress τ_{ij}, on the wall surface is given by,

$$T_i = \tau_{ij} n_j, \tag{7.2}$$

where $\vec{n} = \{n_j\}$ represents the normal to the wall surface. The total traction is then projected along the two local orthonormal tangential directions on the wall surface defined by the resultant wall shear stress. These orthonormal directions are represented by $\vec{l}$ and $\vec{m}$, as discussed previously. The corresponding components of traction or wall shear stresses, τ_l and τ_m, are given by

$$\tau_l = T_i l_i, \tag{7.3}$$

$$\tau_m = T_i m_i. \tag{7.4}$$

The total wall shear stress is given by

$$\tau_w = \sqrt{\tau_l^2 + \tau_m^2}. \tag{7.5}$$

In the present analysis, a completely local investigation is carried out where the wall shear stresses are not projected along the average shear-stress direction, defined by the angle θ in Eq. (3.7). This was done to focus on the local character of the flow, as opposed to investigating quantities that combine elements determined from averages and which could potentially skew the interpretation of the small-scale physical process involved. Irrespective of this choice, Eq. (7.5) is invariant with respect to the use of a local or an average θ.

Iso-contours of total shear stress, τ_w, are shown in figure 23 and 24. In case A, figure 23 shows intermittent streaks of high shear stress between low shear stress. The streaks are mostly aligned along the mean flow direction, as expected. The distribution of high-stress regions appear to be disorganized with no particular large scale coherent pattern, except near the wire contact point where the flow is weaker. This region, which extends roughly

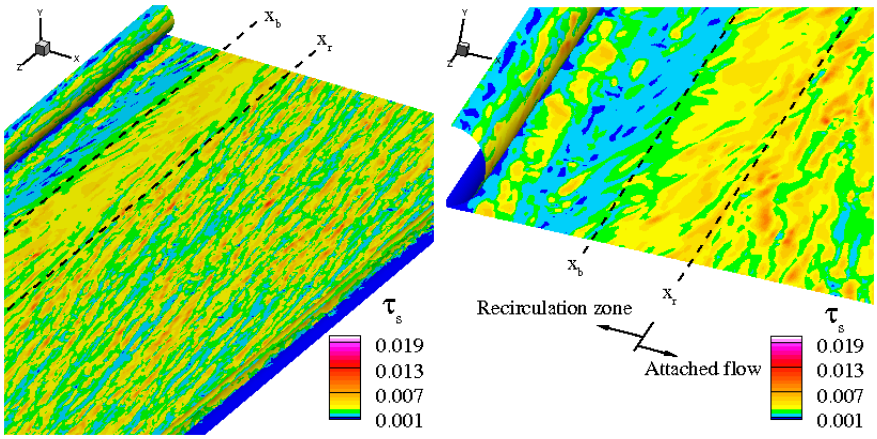

FIGURE 24. Iso-contours of friction stress, τ_w, on the bottom wall including the wire surface for case C. Subfigure (a) contains a large scale view of the wall shear stress while subfigure (b) shows a zoom on the indicated region.

up to 2 wire diameters, contains weaker structures but the qualitative pattern of the shear stress is analogous to that observed in the center of the channel. However, the distribution looks different in case C, where figure 24 shows distinct patterns, or regions, of shear-stress behavior. In the region covering the reattachment zone to the center of the channel, very high shear-stress values are observed. Here, intermittent streaks of high shear stress between low shear-stress regions are observed. The streaks are aligned at an angle with the axial direction owing to the presence of the cross flow. In the recirculation region, the intermittent pattern of shear stress distribution is not as marked since the flow is weaker. The reduced intensity of the streaky structures is similar to that observed in previous studies (Spalart & Coleman 1997; Kaltenbach 2003; Marquillie *et al.* 2008). A sharp change in the magnitude is also observed around the reattachment point. The intermittent or streaky behavior observed towards the center of the channel is similar to the streaky pattern of velocity near the wall observed in a channel flow and turbulent boundary layers Simpson (1996); Kaltenbach (2003). The wall shear stress streaks in both cases seems to align with the mean flow direction. This alignment indicates convection of coherent structures in the net mean flow direction. The presence of these streaks indicates a high level of shear rate which in turn is responsible for production of turbulence kinetic energy near the wall (Kim *et al.* 1987; Kaltenbach 2003). Honkan & Andreopoulos (1997) have also observed similar intermittent behavior in several invariants associated with strain rate and vorticity tensor and have attributed this to a burst of large amplitude events followed by a less violent periods. Near the reattachment, this streaky behavior is reduced owing to the impinging of vortical structures on the wall but the shear stress remains high. The effect of impinging structures is not felt downstream of the reattachment zone as axial flow dominates in that region leading to a fast recovery to the turbulent wall bounded flow, unlike the behavior of unswept separated flows where the flow recovery is slower.

An overlay plot of vortical structures and wall shear stress is shown in figure 25. Instantaneous wall shear stress distribution appears to be well correlated with the shape and orientation of vortical structures. As discussed earlier, wall shear stress shows intermittent regions of high value embedded in low value regions in locations where flow is attached and have regions of reduced magnitude with low and high values in the

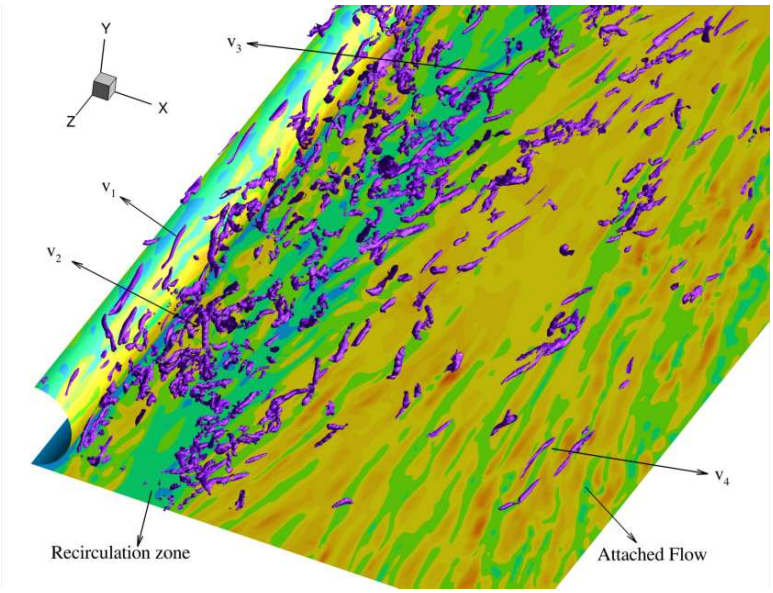

FIGURE 25. Wall shear stress overlayed with vortical structures in the near-wall region for case C identified by $\lambda_2 = -5$. Representative vortical structures are indicated by v_1, v_2, v_3 and v_4.

recirculating zones. Note that on top of the wire, where the flow is mostly attached, quasi-streamwise structures like v_1 are observed. In the regions where flow detaches and forms a shear layer, structures like v_2 are observed with no specific orientation. However close to the wall in the recirculation zone, some slender streamwise structures similar to v_3 are observed. After the flow reattaches itself, quasi-streamwise slender vortices like v_4 are again evident. Thus when wall shear stress assumes intermittent pattern similar to a turbulent channel flow, elongated quasi-streamwise structures are observed. However in regions where wall shear stress changes its distribution due to flow separation, vortical structures also changes their behavior in terms of loosing their specific orientation and shape.

7.1. *Mean and root-mean-square wall shear stress*

The variation of net mean wall shear stress, τ_w defined in Eq. (3.14), as a function of x along the bottom wall is shown in figure 26 for all cases. In case A, τ_w remains fairly constant approximately two diameters away from the wire and decreases gradually as one approaches the wire. As discussed in §5.1, a reduction in axial velocity gradient is observed close to the wire which in turn leads to a reduction in τ_w in this region. In the cases with cross flow, the maximum value of τ_w increases with increasing cross flow. The location of maximum wall shear stress is observed to occur after cross flow reattachment. Away from the wire, where the cross flow is attached, τ_w remains fairly constant. This constant value increases with the amount of cross flow since the resultant mean flowrate increases from case B to D. In the wind-ward side of the wire, τ_w decreases owing to the presence of the secondary recirculation bubble (Dianat & Castro 1991). In the lee-ward side of the wire, it shows a gradual increase with increasing x, reaching a maximum after the mean cross flow reattachment point. This gradual increase is observed in all the cases with cross flow, albeit it is very small in case B. After reaching a peak, τ_w stabilizes to an approximate constant level. The relatively low values of τ_w observed inside the primary and secondary recirculation bubble are similar to observations of Dianat & Castro (1991) and Mittal

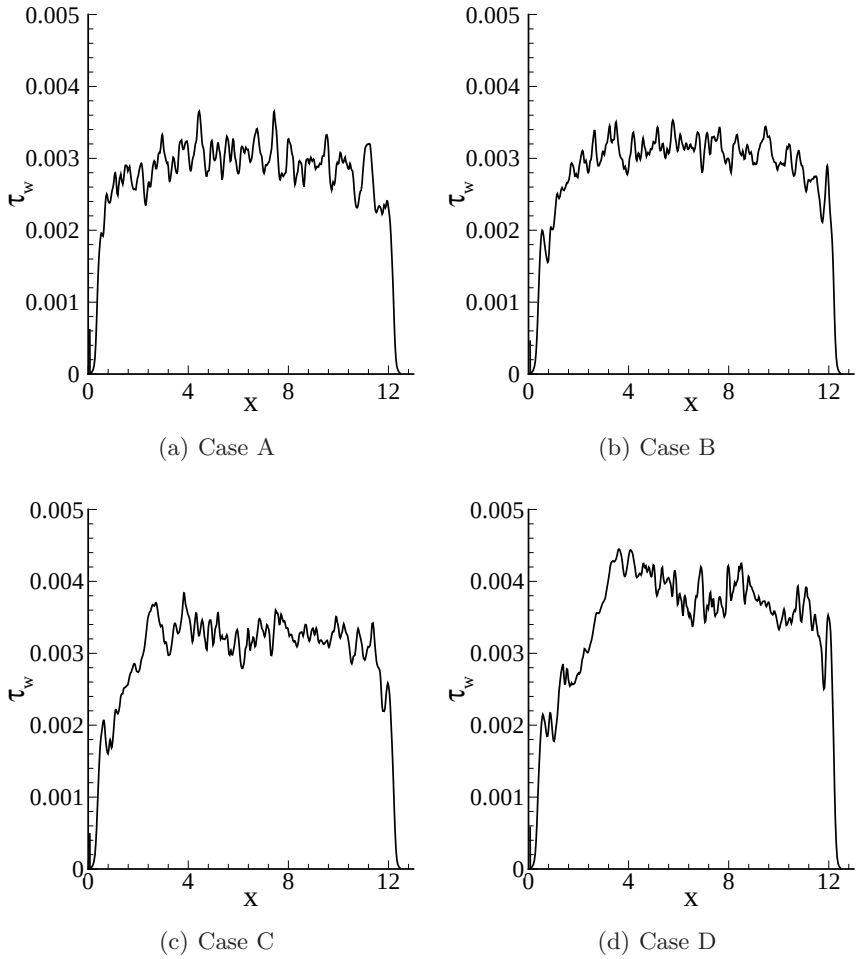

(a) Case A (b) Case B

(c) Case C (d) Case D

FIGURE 26. Variation of mean wall shear stress, τ_w, along cross flow direction for all the cases.

et al. (2003). This behavior is consistent with earlier studies of separating/reattaching flows mentioned in §1, where wall shear stress variation in the streamwise direction has been used to determine reattachment length in separated flows. However in the present case, the criteria of zero wall shear stress at the reattachment location can not be used to determine a reattachment length (Johnston 1970). The zero-crossing of the wall shear stress is a particular condition encountered in unswept flows.

The variation of mean wall shear stress on the wire surface is shown in figure 27 in polar coordinates. The profiles shown corresponds to the mean wall shear stress scaled by a factor of 100 with respect to the zero value denotes by a broken curve. The variation for case A is nearly symmetric, as expected, except close to the contact point of the wire. In the cases with cross flow, symmetry is not observed as cross flow is accelerating in the wind-ward side and decelerating in lee-ward side of the wire. In particular, the value of τ_w is higher in the wind-ward side owing to the flow acceleration and increased wall friction. Overall, the wall shear stress increases with increasing cross flow. Similar profiles are observed in channel flow with a constriction (Mittal *et al.* 2003).

The root-mean squared (r.m.s.) of wall shear stress $\tau_{\mathrm{w,r.m.s.}}$ is shown in figure 28 as a function of x along the bottom wall for all cases. Overall, the dependence of the

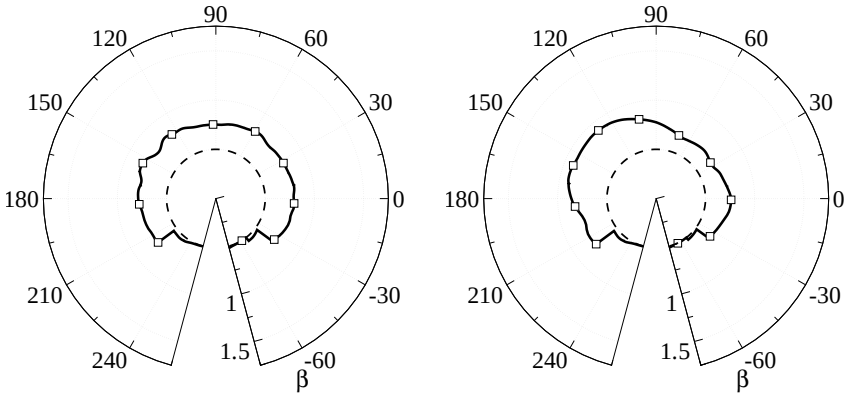

(a) Case A (b) Case B

(c) Case C (d) Case D

FIGURE 27. Variation of mean wall shear stress, τ_w, on the wire surface. The dotted curve indicates the reference level.

r.m.s. of τ_w as a function of x is very similar to that of the mean. Slighter larger r.m.s. values than mean values are observed in case D after reattachment. This is similar to observations near reattachment in earlier studies of separating/reattaching flow (Dianat & Castro 1991; Kaltenbach & Janke 2000; Mittal *et al.* 2003; Li & Naguib 2005). This rise is attributed to impingement of large scale vortical structures in the reattachment region. After reattachment of the flow, a gradual decay and leveling off is observed. It has been suggested that shear stress r.m.s. is correlated with wall-pressure fluctuations (Li & Naguib 2005).

The variation of the r.m.s. of wall shear stress on the wire surface is shown in figure 29 in polar coordinates. The profiles shown corresponds to the r.m.s. values scaled by 500. Nearly symmetric behavior is observed for case A, although some variation is observed which is attributed to slightly lower convergence of these second-order statistics. In the cases with cross flow, the symmetric behavior is lost but there is less resemblance with the mean wall shear stress on the wire surface, as opposed to the behavior on the r.m.s. on the bottom wall which resembles the mean. Relatively speaking, the r.m.s. is more uniformly distributed over the wire surface and large values are not concentrated mostly

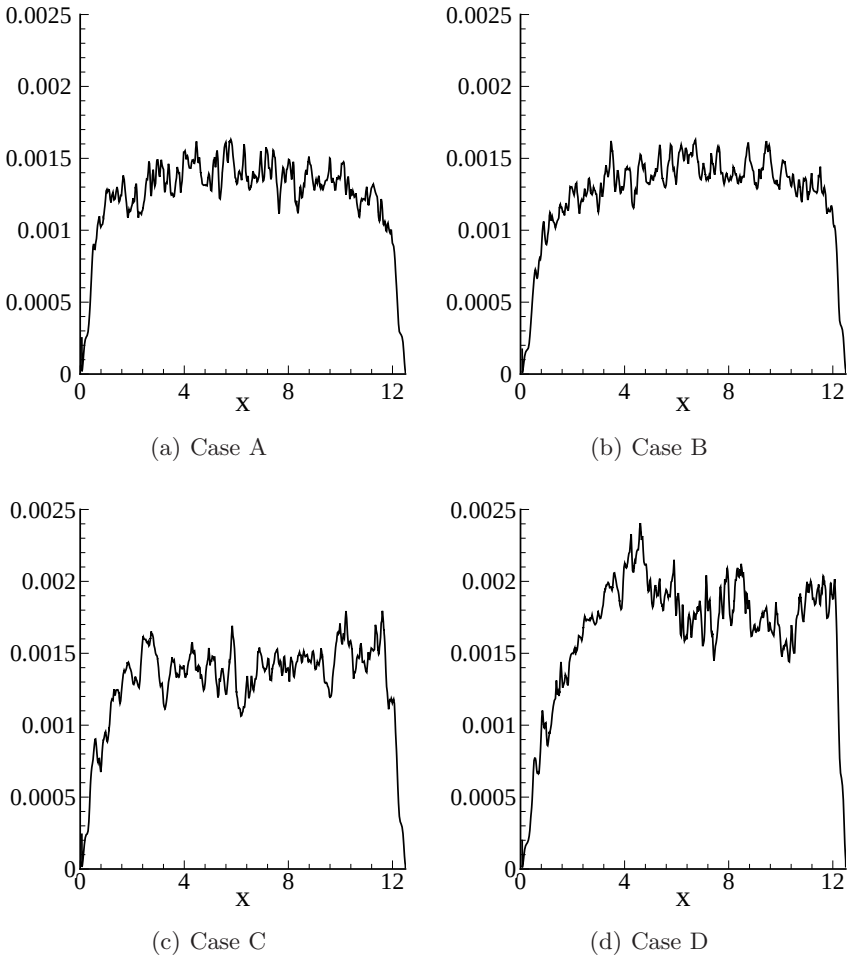

(a) Case A (b) Case B

(c) Case C (d) Case D

FIGURE 28. Variation of $\tau_{\mathrm{w,r.m.s.}}$) along cross flow direction for all the cases.

on the wind-ward side of the wire. In unswept flows, the wall shear stress fluctuations peak on the wind-ward side of the wire and are associated closely with acceleration of mean cross flow (Nepomuceno & Lueptow 1997). Presently, there is substantial axial flow and associated shear stress fluctuations and may explain the observed differences with previous studies.

7.2. *Wall shear stress alignment*

The net mean flow direction is based on a wall shear stress coordinate system, introduced by Simpson (1996). The orientation of wall shear stress with respect to mean flow is important from a modeling point of view. It has been found in previous studies (Johnston 1970; Bradshaw 1987; Webster *et al.* 1996) that the turbulent shear stress is not aligned with the velocity gradient direction, which is an inherent assumptions in isotropic eddy-viscosity models. Appropriate modeling of the near wall region, including anisotropic effects, is believed to be very important for improved simulations based on Reynolds-Averaged Navier-Stokes equations as well as in Large-eddy simulation. The wall shear stress direction tends to be aligned with the turbulent shear stress direction (Simpson 1996). In this section, the variation of the angle between the wall shear stress projections

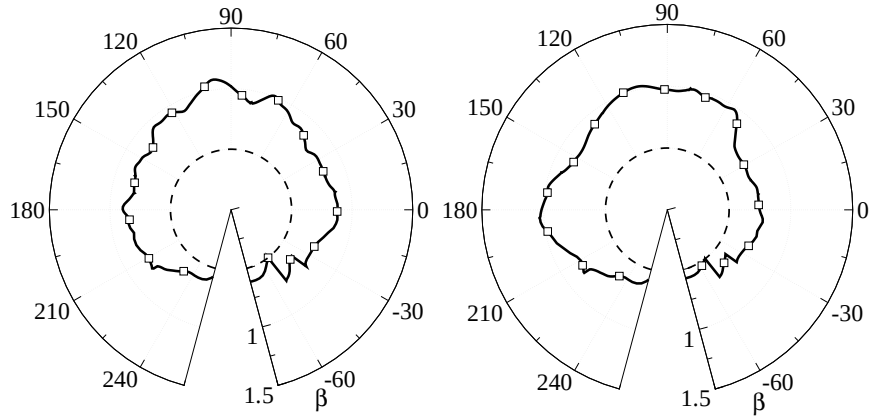

(a) Case A (b) Case B

(c) Case C (d) Case D

FIGURE 29. Variation of r.m.s. of mean wall shear stress, $\tau_{\mathrm{w,r.m.s.}}$, on the wire surface. The dotted curve indicates the reference level.

on the simulation frame of reference is investigated. The angle between the wall shear stress components $\langle\tau_{mn}\rangle$ and $\langle\tau_{ln}\rangle$ is defined by Eq. (3.7). This is a mean angle defined by averaging along the homogeneous z direction. The variation of this angle as a function of x on the bottom wall is shown in figure 30 for all cases. The angle is very small in case A because there is no cross flow; the shear stress vector is mostly aligned along the axial direction. For the cases with cross flow, negative values of angle θ are observed in the lee-ward side of the wire. This is a consequence of the mean cross flow reversal within the recirculation zone. The absolute vale θ increases with increasing cross flow. After flow reattachment, the angle becomes positive and increases with increasing x until the secondary recirculation bubble in the wind-ward side of the wire is reached. Within this last region, the angle changes sign for the same reason explained before for the primary recirculation zone. The variation observed in θ is consistent with the mean wall shear stress variation shown in figure 26. Moreover, θ could be used to define the reattachment length, as the point where θ becomes zero, and it could be viewed as a generalization of the zero wall-shear stress condition used in unswept flows. Another feature of θ is that it is indicative of the degree of flow recovery after reattachment. As observed in figure 30,

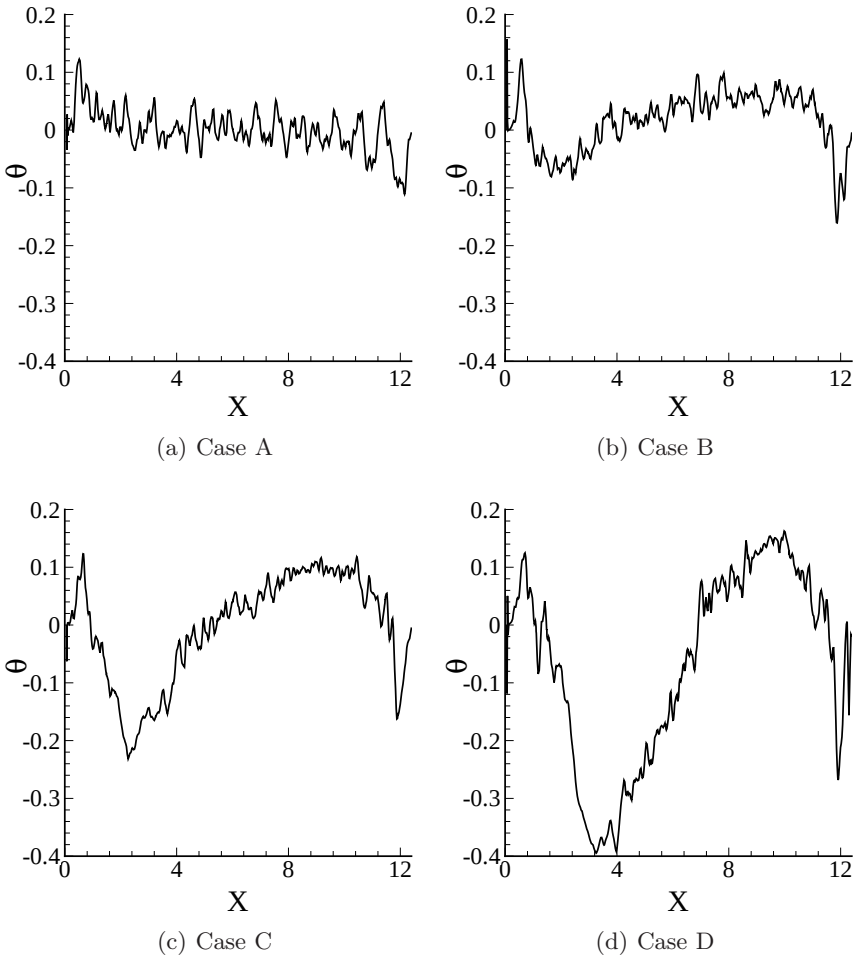

(a) Case A (b) Case B

(c) Case C (d) Case D

FIGURE 30. Variation of angle θ along cross flow direction for all the cases.

there is barely enough space for the flow to recover in case D with the domain size utilized in the present study.

The variation of θ on the wire surface is shown in figure 31. The profiles shown correspond to $0.5(\pi + \theta)$. In these plots, the corner regions of the wire are excluded because appropriate convergence of the mean shear stresses could not be realized; θ exhibited too large fluctuations there. In all cases with cross flow, an increase in θ is observed in the wind-ward side of the wire, with a maximum values in the region ($90^o < \beta < 180^o$). These maximum values are correlated with the increasing cross flow. Moreover, little variation is observed in the lee-ward side of the wire. Here, the wall shear stress, $\langle \tau_{mn} \rangle$, is quite small. The variation of θ on the wire surface is consistent with the mean wall shear stress variation shown in figure 27.

7.3. *Shear stress probability density function*

The shear-stress distribution was investigated qualitatively by considering the iso-contours on the wall surface and it is now investigated quantitatively by their probability density function (p.d.f.). These p.d.f.s are extracted from the data in the homogeneous axial direction. Case A and C have been chosen as the reference flows without and with cross

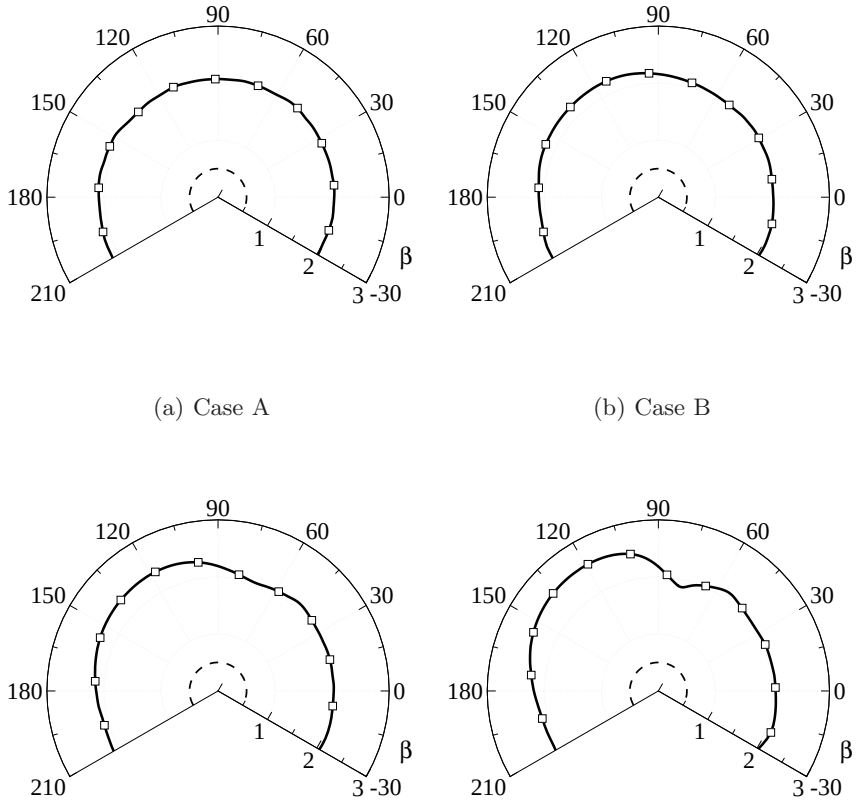

(a) Case A (b) Case B

(c) Case C (d) Case D

FIGURE 31. Variation of θ on the wire surface. The dotted curve indicates the reference level.

Case	Location	mean	r.m.s.	ratio	skewness	kurtosis
A	x_d	0.0027	0.00098	0.37	0.80	3.48
	1.97	0.0034	0.00120	0.36	1.30	6.05
	2.70	0.0030	0.00110	0.37	1.22	5.82
	3.50	0.0031	0.00100	0.34	0.97	5.25
	4.30	0.0031	0.00120	0.38	1.18	5.52
	x_c	0.0028	0.00110	0.39	1.18	4.65
C	x_R	0.0021	0.00071	0.34	1.11	5.12
	x_b	0.0025	0.00110	0.46	1.19	4.94
	2.70	0.0029	0.00087	0.30	1.41	6.82
	3.50	0.0032	0.00089	0.28	1.24	5.96
	x_r	0.0032	0.00088	0.27	1.17	5.20
	5.00	0.0033	0.00100	0.31	1.20	5.31

TABLE 5. Statistical parameters of maximum wall shear stress.

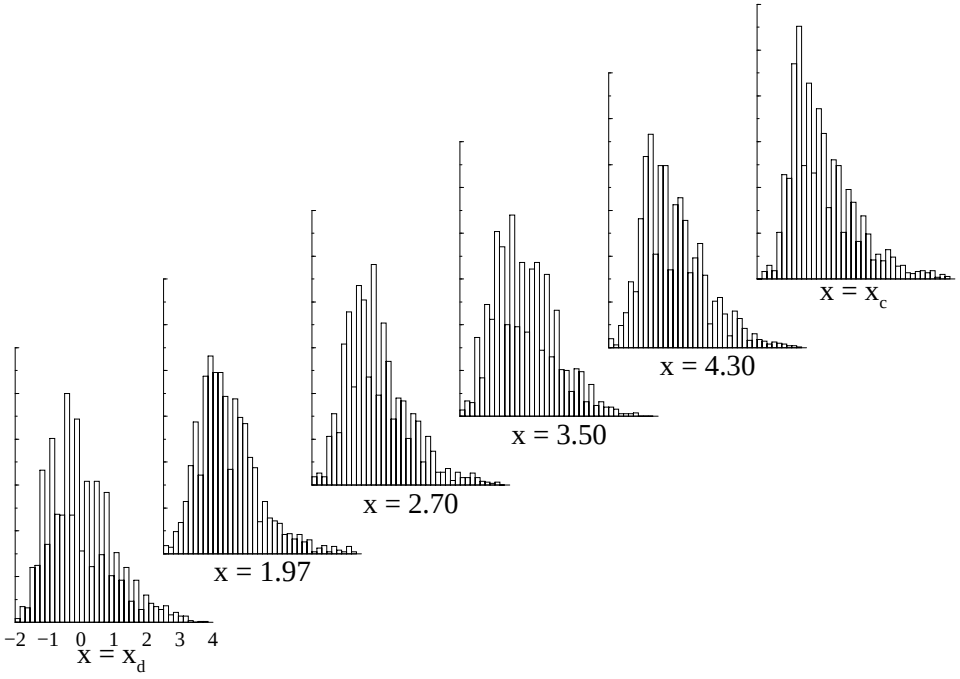

FIGURE 32. P.d.f.s of normalized shear stress, $\tau_w^{'}$, for case A at different locations.

flow. The p.d.f.s are discussed at six different cross flow locations, given in Table 5 with their respective first two moments. The locations x_d and x_c corresponds to $x = 2R$ and the center of the channel, respectively, whereas locations x_b and x_r were defined previously. For case C, additional locations have been chosen to better understand the behavior of the p.d.f. around the reattachment line. These same locations are also used to extract the p.d.f. for case A.

The p.d.f. of normalized wall shear stress, $\tau_w^{'} = (\tau_w - \langle\tau_w\rangle)/\tau_{\mathrm{w,r.m.s.}}$, is obtained at the six different cross flow locations indicated in Table 5. These p.d.f.s are shown in figure 32 and 33. The statistical moments of τ_w are summarized in Table 5. For case A, the ratio of mean, root-mean-square, skewness and flatness factor at x_c, the center of channel, is in agreement with the previous experimental and numerical results summarized in Obi *et al.* (1996). Near the wire, x_R, the skewness and kurtosis values are lower than at the center of channel. This implies that the intermittency of the shear stress is lower closer to the wire. This is also observed in figure 23(a), where the high shear stress streaks in close proximity with the wire appear to be less frequent than in the region around the center of the channel. Away from x_R, mean, root-mean-square, skewness and kurtosis increase and then decrease towards the center of the channel. This behavior is caused by the wire. The profiles obtained at all the locations are positively skewed and have high kurtosis indicating presence of less frequent high wall shear stress events. For case C, before the center of the primary recirculation bubble, the skewness and kurtosis are slightly lower compared to the locations after the center of bubble. This indicates slight reduction in frequency of high amplitude bursts in this region (Singh & Azad 1995). At locations lying between the center of the primary recirculation bubble and the reattachment line, the skewness and kurtosis are higher in comparison to the values at the center of the channel owing to the turbulent flow being more energetic near the reattachment region. In figure 24, the wall shear stress under the primary recirculation

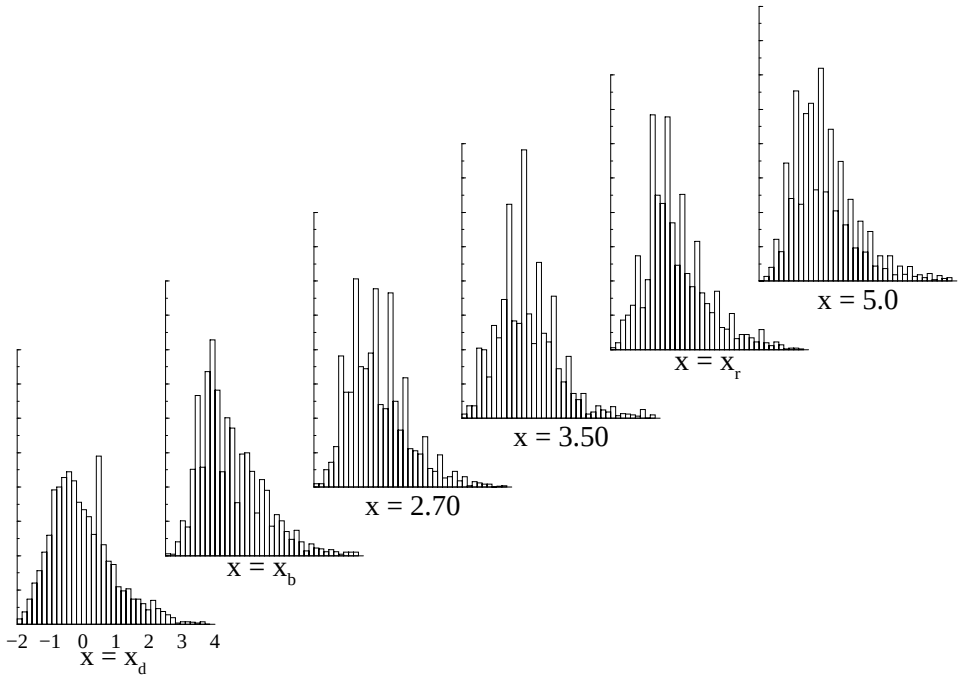

FIGURE 33. P.d.f.s of normalized shear stress, $\tau_w^{'}$, for case C at different locations.

bubble shows a sudden change from low to high values. Intermittency is higher compared to the center of the channel leading to larger values of the kurtosis. These results are similar to those observed in flow over a backward-facing step (Simpson 1996) where the first half of the primary recirculation bubble is found to be less energetic compared to the second half that is closer to the reattachment zone. However, the variation observed in skewness and kurtosis in case C is substantially less than that in a backward-facing step in the recirculation region as the flow is fully turbulent inside the bubble owing to presence of axial turbulent flow. After reattachment, at x_r, the skewness value is similar to that in the center of the channel but the kurtosis is higher. This is again caused by the sudden change in wall shear stress distribution in the region near the zone of reattachment, causing an increase in intermittent behavior as the flow unsteadily traverses this zone separating the recirculation bubble from the main flow in the channel. As discussed earlier in §5.1, the reattachment region is in a highly non-equilibrium state characterized by large unsteadiness from impingement of vortical structures. This results in the high kurtosis levels observed in this region. Similar to case A, all the p.d.f. profiles are positively skewed with high kurtosis levels compared to a Gaussian distribution, which indicates the presence of unfrequent high amplitude shear stress events.

8. Conclusions

Acknowledgment

This work was supported in part by Argonne National Laboratory under subcontract 7F-01201 and by the Center for the Simulation of Advanced Rockets supported by the U.S. Department of Energy through the University of California under subcontract B523819. This research used resources of the Argonne Leadership Computing Facility at Argonne

National Laboratory, which is supported by the Office of Science of the U.S. Department of Energy under contract DE-AC02-06CH11357.

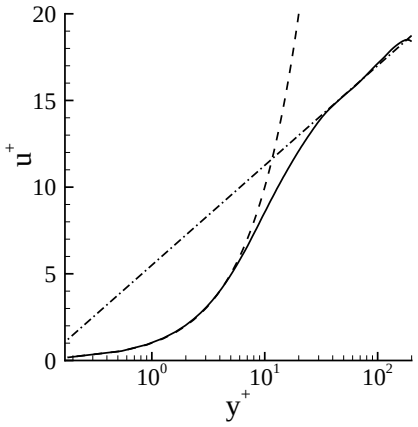

FIGURE 34. Profile of mean streamwise velocity normalized with wall shear velocity, compared with law of the wall. Solid line is simulation data, dashed line is $u^+ = y^+$ and dashed-dotted line is $u^+ = 2.5\ lny^+ + 5.5$.

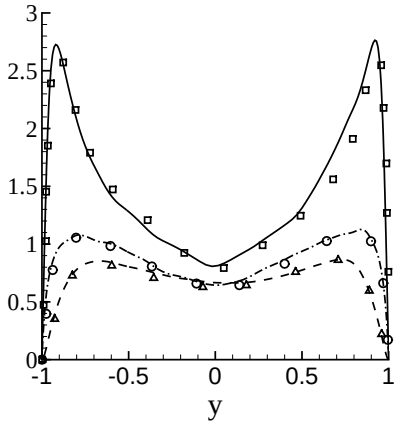

FIGURE 35. Profile of turbulence intensity compared with DNS results of Kim *et al.* (1987). Symbols (□), (Δ) and (○) denote DNS data of Kim *et al.* (1987) whereas lines denotes simulation data for u_{rms}, v_{rms} and w_{rms} respectively. Solid line is u_{rms}, dashed line is v_{rms} and dashed-dotted line is w_{rms}.

Appendix A. Validation

The code was validated against the reference DNS of Kim *et al.* (1987). This corresponds to a simulation of turbulent channel flow at Reynolds number of 3300 based on center line velocity and friction Reynolds number of 180. The simulation is performed using the same numerical procedure detailed in section 3.1, with a total of approximately 4 million grid points collocated in the same manner as that used in Kim *et al.* (1987). The mean velocity profile obtained from the validation simulation, the reference DNS and compared with the reference "Law of the Wall" described in the main body of the manuscript is shown in figure 34. The turbulence intensity profiles compared with results from the reference DNS are shown in figure 35. Excellent and good agreement is observed in the mean velocity and turbulence intensity profiles, respectively.

REFERENCES

Achraya, S., Dutta, S., Myrum, T. A. & Baker, R. S. 1994 Turbulent flow past a surface-mounted two-dimensional rib. *J. Fluids Eng.* **116**, 238–246.

Adams, E. W. & Johnston, J. P. 1988 Effects of the separating shear layer on the reattachment flow structure part 2: Reattachment length and wall shear stress. *Exp. in Fluids* **6**, 493–499.

Angele, K. P. & Muhammad-Klingmann, B. 2006 PIV measurements in a weakly separating and reattaching turbulent boundary layer. *European Journal of Mechanics - B/Fluids* **25** (2), 204 – 222.

Armaly, B. F., Durst, F., Pereira, J. C. F. & Schonung, B. 1983 Experimenat and theoretical investigation of backward-facing step flow. *J. Fluid Mech.* **127**, 473–496.

Bradshaw, P. 1987 Turbulent secondary flows. *Ann. Rev. Fluid Mech.* **19**, 53–74.

Bradshaw, P. & Wong, F. 1972 The reattachment and relaxation of a turbulent shear layer. *J. Fluid Mech.* **52**, 113–135.

Camussi, R., Felli, M., Pereira, F., Aloisio, G. & Marco, A. D. 2008 Statistical properties of wall pressure fluctuations over a forward-facing step. *Physics of Fluids* **20**, 075113.

Caruelle, B.and Ducros, F. 2003 Detached-eddy simulations of attached and detached boundary layers. *International Journal of Computational Fluid Dynamics* **17**, 433–451(19).

Chun, S., Liu, Y. Z. & Sung, H. J. 2004 Wall pressure fluctuations of a turbulent separated and reattaching flow affected by an unsteady wake. *Exp. in Fluids* **37**, 531–546.

Chun, S. & Sung, H. J. 2003 Large-scale vortical structure of turbulent separation bubble affected by unsteady wake. *Exp. in Fluids* **34**, 572–584.

Deck, S. & Thoringy, P. 2007 Unsteadiness of an axisymmetric separating-reattaching flow: Numerical investigation. *Physics of Fluids* **19**, 065103.

Dejoan, A. & Leschziner, M. A. 2004 Large eddy simulation of periodically perturbed separated flow over a backward-facing step. *International Journal of Heat and Fluid Flow* **25** (4), 581 – 592.

Dianat, M. & Castro, I. P. 1991 Turbulence in a separated boundary layer. *J. Fluid Mech.* **226**, 91–123.

Dwight, B., Gomes, M. G. M. & D., H. R. 2002 Three-dimensional instability in flow over a backward-facing step. *J. Fluid Mech.* **473**, 167–190.

Eaton, J. K. & Johnston, J. P. 1981 A review of research on subsonic turbulent flow reattachment. *AIAA J.* **19**, 1093–1100.

Farabee, T. M. & Casarella, M. J. 1986 Measurements of fluctuating wall pressure for separated/reattached boundary layer flows. *Journal of vibration, acoustis, stress, and reliability in design* **108**, 301–307.

Fröhlich, J., Mellen, C., P., Rodi, W., Temmerman, L. & Leschziner, M., A. 2005 Highly resolved large-eddy simulation of separated flow in a channel with streamwise periodic constrictions. *J. Fluid Mech.* **526**, 19–66.

Gallaire, F., Marquillie, M. & Ehrenstein, U. 2007 Three-dimensional transverse instabilities in detached boundary layers. *J. Fluid Mech.* **571**, 221–233.

Griffith, M. D., Thompson, M. C., Leweke, T., Hourigan, K. & P., A. W. 2007 Wake behaviour and instability of flow through a partially blocked channel. *J. Fluid Mech.* **582**, 319–340.

Henderson, R. D. 1994 Unstructured spectral element methods: Parallel algorithms and simulations. PhD thesis, Princeton University.

Henderson, R. D. & Karniadakis, G. E. 1995 Unstructured spectral element methods for simulation of turbulent flows. *J. Comp. Phys.* **122**, 191–217.

Hoarau, C., Borée, J., Laumonier, J. & Gervais, Y. 2006 Analysis of the wall pressure trace downstream of a separated region using extended proper orthogonal decomposition. *Physics of Fluids* **18**, 055107.

Honkan, A. & Andreopoulos, Y. 1997 Vorticity, strain-rate and dissipation characteristics in the near-wall region of turbulent boundary layers. *J. Fluid Mech.* **350** (-1), 29–96.

Hudy, L. M., Naguib, A. & Humphreys, W. M. 2003 Wall-pressure-array measurements beneath a separating-reattaching flow region. *Physics of Fluids* **15**, 706.

Hudy, L. M., Naguib, A. & Humphreys, W. M. 2007 Stochastic estimation of a separated-flow field using wall-pressure-array measurements. *Physics of Fluids* **19**, 024103.

Hwang, R. R., Chow, Y. C. & Peng, Y. F. 1999 Numerical study of turbulent flow over two-dimensional surface mounted ribs in a channel. *I. J. for Numer. Meth. Fluids.* **31**, 767–785.

Jeong, J. & Hussain, F. 1995 On the identification of a vortex. *J. Fluid Mech.* **285**, 69–94.

Jeong, J., Hussain, F., Schoppa, W. & Kim, J. 1997 Coherent structures near the wall in a turbulent channel flow. *J. Fluid Mech.* **332**, 185–214.

Johnston, J. P. 1970 Measurements in a 3-dimensional turbulent boundary layer induced by a swept, forward facing step. *J. Fluid Mech.* **42**, 823–844.

Kaiktsis, L. & Monkewitz, P. A. 2003 Global destabilization of flow over a backward-facing step. *Physics of Fluids* **15**, 3647.

Kaltenbach, H.-J. 2003 The effect of sweep-angle variation on the turbulence structure in a separated, three-dimensional flow. *Theor. Comput. Fluid Dynamics* **16** (3), 187–210.

Kaltenbach, H.-J. & Janke, G. 2000 Direct numerical simulation of flow separation behind a swept, rearward-facing step at $Re_H = 3000$. *Physics of Fluids* **12**, 2320.

Karniadakis, G. E. 1999 Simulating turbulence in complex geometries. *Fluid Dynamics Research* **24**, 343–362.

Karniadakis, G. E., Israeli, M. & Orszag, S. A. 1991 High-order splitting methods for the incompressible Navier-Stokes equations. *J. Comp. Phys.* **97**, 414–443.

Kays, W. M. & Crawford, M. E. 2004 *Convective Heat and Mass Transfer*. McGraw Hill.

Kiel, R. & Vieth, D. 1995 Experimental and theoretical investigations of the near-wall region in a turbulent separated and reattached flow. *Experimental Thermal and Fluid Science* **11** (3), 243 – 254.

Kim, J., Moin, P. & Moser, R. 1987 Turbulence statistics in fully developed channel flow at low Reynolds number. *J. Fluid Mech.* **177**, 133–166.

Kim, J. & Sung, H. J. 2006 Wall pressure fluctuations in a turbulent boundary layer over a bump. *AIAA J.* **44** (7), 1393–1401.

Kiya, M. & Sasaki, K. 1985 Structure of large-scale vortices and unsteady reverse flow in the reattaching zone of a turbulent separation bubble. *J. Fluid Mech.* **154**, 463–491.

Laskowski, G. M. & Durbin, P. A. 2007 Direct numerical simulations of turbulent flow through a stationary and rotating infinite serpentine passage. *Physics of Fluids* **19**, 015101.

Le, H., Moin, P. & Kim, J. 1997 Direct numerical simulation of turbulent flow over a backward-facing step. *J. Fluid Mech.* **330**, 349–374.

Lee, I. & Sung, H. J. 2002 Multiple-arrayed pressure measurement for investigation of the unsteady fow structure of a reattaching shear layer. *J. Fluid Mech.* **463**, 377–402.

Li, Y. & Naguib, A. M. 2005 High-frequency oscillating-hot-wire sensor for near-wall diagnostics in separated flows. *AIAA J.* **43** (3), 520–529.

Liu, Y. Z., Kang, W. & Sung, H. J. 2005 Assessment of the organization of a turbulent separated and reattaching flow by measuring wall pressure fluctuations. *Exp. in Fluids* **38**, 485–493.

Liu, Y. Z., Ke, F., Chen, H. P. & Sung, H. J. 2006 A wall-bounded turbulent mixing layer flow over an open step: I. time-mean and spectral characteristics. *Journal of Turbulence* **7** (65), 1 – 17.

Liu, Y. Z., Ke, F., Chen, H. P. & Sung, H. J. 2007 A wall-bounded turbulent mixing layer flow over an open step: part 2. unsteady characteristics. *Journal of Turbulence* **8** (26), 1 – 17.

Liua, Y. Z., Ke, F. & Sung, H. J. 2008 Unsteady separated and reattaching turbulent flow over a two-dimensional square rib. *Journal of Fluids and Structures* **24**, 366–381.

Lu, G. & Lele, S. K. 1993 Inviscid instability of a skewed compressible mixing layer. *J. Fluid Mech.* **249**, 441–463.

Marquillie, M. & Ehrenstein, U. 2003 On the onset of nonlinear oscillations in a separating boundary-layer flow. *J. Fluid Mech.* **490**, 169–188.

Marquillie, M., Laval J., P. & Dolganov, R. 2008 Turbulence characteristics of a boundary layer over a two-dimensional bump. *Journal of Turbulence* **9**, 1–23.

Mellen, C. P., Fröhlich, J. & Rodi, W. 2000 Large eddy simulation of the flow over periodic hills. In *Proc. IMACS World Congress* (ed. M. Deville & R. Owens). Lausanne.

Mittal, R., Simmons, S. P. & Najjar, F. 2003 Numerical study of pulsatile flow in a constricted channel. *J. Fluid Mech.* **485**, 337–378.

Moin, P. & Mahesh, K. 1998 Direct numerical simulation: A tool in turbulence research. *Ann. Rev. Fluid Mech.* **30**, 539–578.

Muppidi, S. & Mahesh, K. 2007 Direct numerical simulation of round turbulent jets in cross-flow. *J. Fluid Mech.* **574**, 59–84.

Na, Y. & Moin, P. 1998 Direct numerical simulation of a turbulent boundary layer. *J. Fluid Mech.* **374**, 379–405.

Nepomuceno, H. G. & Lueptow, M. 1997 Pressure and shear stress measurements at the wall in a turbulent boundary layer on a cylinder. *Physics of Fluids* **9**, 2732.

Nickels, T. 2004 Inner scaling for wall-bounded flows subject to large pressure gradients. *J. Fluid Mech.* **521**, 217–239.

Obi, S., Inoue, K., Furukawa, T. & Masuda, S. 1996 Experimental study on the statistics of wall shear stress in turbulent channel flow. *I. J. of Heat and fluid Flow* **17**, 187–192.

Peller, N. & Manhart, M. 2006 *New Results in Numerical and Experimental Fluid Mechanics V*. Springer Berlin / Heidelberg.

Rajagopalan, S. & Antonia, R. A. 1993 Structure of the velocity field associated with the spanwise vorticity in the wall region of a turbulent boundary layer. *Phys. Fluids A* **5** (10), 2502.

Rani, H. P., Sheu, T. W. H. & Tsai, E. S. F. 2007 Eddy structures in a transitional backward-facing step flow. *J. Fluid Mech.* **588**, 43–58.

Rodi, W. 2006 High performance computation for DNS/LES. *Fluid Dynamics Research* **38**, 145–173.

Sadeque, M. A. F., Rajaratnam, N. & Loewen, M. R. 2008 Flow around cylinders in open channels. *Journal of Engineering Mechanics* **134** (1), 60–71.

Schumann, U. 1975 Subgrid scale model for finite difference simulations of turbulent flows in plane channels and annuli. *J. Comput. Phys.* **18**, 376–404.

Sheu, T. W. H. & Rani, H. P. 2006 Exploration of vortex dynamics for transitional flows in a three-dimensional backward-facing step channel. *J. Fluid Mech.* **550**, 61–83.

Shih, C. & Ho, C.-M. 1994 Three-dimensional recirculating flow in a backward facing step. *J. Fluids Eng.* **116**, 228–232.

Simpson, R. L. 1996 Aspects of turbulent boundary-layer separation. *Prog. Aerospace Sci.* **32**, 457–521.

Singh, R. K. & Azad, R. S. 1995 Behavior of mean and fluctuating skin friction in a conical diffuser with instantaneous flow reversals. *Experimental Thermaland Fluid Science* **11**, 190–203.

Snarski, S. R. & Lueptow, R. M. 1995 Wall pressure and coherent structures in a turbulent boundary layer on a cylinder in axial flow. *J. Fluid Mech.* **286**, 137–171.

Song, S. & Eaton, J. K. 2004 Flow structures of a separating, reattaching, and recovering boundary layer for a large range of Reynolds number. *Exp. in Fluids* **36**, 642–653.

Spalart, P. R. & Coleman, G. N. 1997 Numerical study of a separation bubble with heat transfer. *European Journal of Mechanics - B/Fluids* **16** (2), 169 – 189.

Spalart, P. R. & Strelets, M. K. 2000 Mechanisms of transition and heat transfer in a separation bubble. *Journal of Fluid Mechanics* **403** (-1), 329–349.

Weber, D. J. & Danberg, J. E. 1992 Correlation of mean velocity measurements downstream of a swept backward-facing step. *AIAA J.* **30**, 2701–2706.

Webster, D., R., DeGraaf D., B. & Eaton, J., K. 1996 Turbulence characteristics of a boundary layer over a swept bump. *J. Fluid Mech.* **323**, 1–22.

Wilhelm, D., Härtel, C. & Kleiser, L. 2003 Computational analysis of the two-dimensional–three-dimensional transition in forward-facing step flow. *J. Fluid Mech.* **489**, 1–27.

Wood, D. H. & Bradshaw, P. 1982 A turbulent mixing layer constrained by a solid surface. part 1. measurements before reaching the surface. *J. Fluid Mech.* **122**, 57–89.

Wu, X., A. & Squires K., D. 1998 Numerical investigation of the turbulent boundary layer over a bump. *J. Fluid Mech.* **362**, 229–271.

Zang, T. A. 1991 On the rotational and skew-symmetric forms for incompressible flow simulations. *App. Num. Math* **7**, 27–40.